energies

MDPI

Article

Representation of Tidal Turbine Support Structures in a Regional-Scale 3D Hydrodynamic Model and Their Effects on Wake Prediction

Raymond Lam *, Nairn Spence, Tian Tan, Chris Old and Brian Sellar

School of Engineering, Institute for Energy Systems, The University of Edinburgh, Edinburgh EH9 3DW, UK
* Correspondence: raymond.lam@ed.ac.uk

Abstract

Tidal turbine wake predictions in regional-scale hydrodynamic models typically account for rotor thrust but neglect the drag of support structures. This study introduces a method for representing turbine support structures as permeable drag volumes within TELEMAC-3D and evaluates their influence on wake characteristics. The method is demonstrated for the 1 MW DeepGen-IV turbine deployed at the Fall of Warness test site at the European Marine Energy Centre, Scotland. The tripod foundation, tower, and nacelle are each implemented as momentum source terms alongside an actuator disc rotor in a regional-scale model with mesh resolution down to 1.5 m with 24 sigma layers and output at 60 s intervals (1 s at instrument locations), validated against seabed-mounted ADCP measurements. Including the support structures improves the agreement with measured wake profiles by 6–18% in root-mean-square error at 3.7 rotor diameters downstream and extends the hub-height 5% velocity deficit distance by an average of three rotor diameters (∼54 m), with substantial variability across tidal conditions. The tripod and tower drag also extend the velocity deficit into the lower water column, a feature absent from the rotor-only formulation, with potential relevance to near-bed processes such as bed shear stress and sediment transport which are not examined in the present study. The implementation is in principle extendable to other support concepts and multi-device studies, and the results indicate that support structure drag should be considered in regional wake models where wake persistence and downstream interactions are important.

Keywords: tidal stream turbine; support structures; tidal turbine wake modelling; regional hydrodynamic model; TELEMAC-3D; Acoustic Doppler Current Profiler (ADCP)

Academic Editor: Tonio Sant

Received: 1 May 2026
Revised: 25 May 2026
Accepted: 1 June 2026
Published: 4 June 2026

1. Introduction

Tidal stream energy is increasingly regarded as a credible contributor to future low-carbon electricity systems because of the predictability of tidal flows and the concentration of resource in coastal channels. As the sector progresses from single-device demonstrations toward larger deployments [1–6], accurate prediction of turbine wakes becomes increasingly important for array layout, downstream performance, fatigue loading, and environmental assessment [7,8]. Experimental and field studies have characterised the structure, recovery, and inter-turbine interaction of tidal turbine wakes under varying conditions [9–12], providing measurements against which numerical wake predictions can be validated.

Most regional wake studies represent turbines using actuator disc or momentum sink approaches that account for rotor thrust but neglect the drag of support structures [13–15].

This simplification may be reasonable when only bulk thrust effects are of interest, but tidal energy converters (TECs) also include foundations, towers, nacelles, and, in some cases, floating hulls and mooring systems that interact with the flow independently of the rotor.

Previous experimental, numerical, and theoretical studies indicate that support structures can materially affect wake behaviour. Reported effects include changes in turbine performance [16,17], enhanced turbulence production [18], asymmetric wake recovery [19], altered vorticity structure and increased near-bed flow modification [20]. These findings suggest that neglecting support structure drag may bias wake predictions, particularly where wake recovery distance or vertical wake structure is important. However, support structures are rarely represented explicitly in regional-scale three-dimensional (3D) hydrodynamic models, and their influence on wake prediction at that scale has not yet been evaluated.

High-fidelity Computational Fluid Dynamics (CFD) approaches, including Detached Eddy Simulation (DES) and Large-Eddy Simulation (LES) with explicitly resolved tower and foundation geometry, characterise the flow–structure interaction in detail [21,22], but their computational expense restricts them to small domains and short-duration simulations. Regional-scale three-dimensional hydrodynamic models address the complementary requirement of representing channel-wide bathymetry, tidal forcing, and array-scale flow interactions over longer time and spatial scales relevant to array layout, environmental assessment, and yield estimation. Within regional-scale free-surface solvers of this class, fully resolved geometries of the support structures are not numerically possible for components suspended in the water column (such as the nacelle, or the hull of floating devices), and are impractical for bottom-mounted components such as the tripod and tower, where the sigma-coordinate vertical discretisation does not accommodate the sharp vertical walls required for geometric fidelity.

In this study, we introduce a permeable drag volume method, which represents each support component through a prescribed frontal area, drag coefficient, and discretised volume, and addresses these constraints within TELEMAC-3D. We assess its influence on wake characteristics behind the 1 MW DeepGen-IV turbine deployed at the European Marine Energy Centre, Fall of Warness, Scotland. The rotor is represented as an actuator disc, while the tripod foundation, tower, and nacelle are modelled as permeable drag volumes with prescribed drag coefficients. The method is implemented in a high-resolution 3D regional model and evaluated against seabed-mounted Acoustic Doppler Current Profiler (ADCP) measurements using three simulation cases: ambient flow without the turbine, rotor-only, and rotor plus support structures. The rotor-only case represents the conventional treatment of tidal turbines in regional-scale models and provides the baseline against which the contribution of the support structures is assessed.

2. Methodology

2.1. TELEMAC-3D and Its Governing Equations

TELEMAC-3D is a validated hydrodynamic module from the TELEMAC open-source suite primarily developed by the EDF R&D to model regional-scale tidal current flows. TELEMAC-3D solves the free-surface, incompressible, unsteady Reynolds-Averaged Navier–Stokes (RANS) equations in 3D, capturing flow variations in the vertical direction. TELEMAC-3D also provides an option to include dynamic pressure in the governing equations, i.e., a non-hydrostatic model formulation, which is important when modelling flows over steep slopes and is used in this study. TELEMAC-3D allows user-defined source terms through custom subroutines (specifically the `USER_SOURCE` subroutine), which enables implementation of turbine rotor thrust and support structure drag in the present study.

The continuity and momentum equations being solved are

$$\frac{\partial U}{\partial x} + \frac{\partial V}{\partial y} + \frac{\partial W}{\partial z} = 0 \quad (1)$$

$$\frac{\partial U}{\partial t} + U\frac{\partial U}{\partial x} + V\frac{\partial U}{\partial y} + W\frac{\partial U}{\partial z} = -\frac{1}{\rho}\frac{\partial p}{\partial x} + v\Delta(U) + F_x \quad (2)$$

$$\frac{\partial V}{\partial t} + U\frac{\partial V}{\partial x} + V\frac{\partial V}{\partial y} + W\frac{\partial V}{\partial z} = -\frac{1}{\rho}\frac{\partial p}{\partial y} + v\Delta(V) + F_y \quad (3)$$

$$\frac{\partial W}{\partial t} + U\frac{\partial W}{\partial x} + V\frac{\partial W}{\partial y} + W\frac{\partial W}{\partial z} = -\frac{1}{\rho}\frac{\partial p}{\partial z} + v\Delta(W) + F_z \quad (4)$$

where U, V, and W are the 3D components of velocity in the horizontal (x and y) and vertical (z) directions respectively. v is the kinematic viscosity and tracer diffusion coefficient, t is the time, p is the pressure and ρ is the water density (ρ = 1025 kg/m^3). F_x, F_y and F_z are source terms denoting the wind, the Coriolis force and the bottom friction or any other physical processes being modelled, including the drag forces of the turbine rotor and its support structures.

The pressure is split up into hydrostatic pressure and dynamic pressure terms:

$$p = p_{atm} + \rho_0 g(Z_s - z) + \rho_0 g \int_z^{Z_s} \frac{\Delta\rho}{\rho_0} dz + p_d \quad (5)$$

where p_{atm} is the atmospheric pressure, g is the acceleration due to gravity (g = 9.81 m/s^2), Z_s is the free-surface elevation, ρ_0 is the reference water density, $\Delta\rho$ is the variation in density around the reference density and p_d is dynamic pressure.

Further details on the theoretical basis of TELEMAC-3D including basic algorithms and model verification details can be found in [23,24], while the full derivation of Equations (1) to (5) is described further in [25].

2.2. Turbine Specifications

The tidal energy converter (TEC) considered in this study is the 1MW, three-bladed, horizontal-axis DeepGen-IV tidal turbine. Figure 1 shows the 3D TEC model and the TEC being deployed from Orkney, Scotland, as part of the Reliable Data Acquisition Platform for Tidal (ReDAPT) project conducted between 2012 and 2014. The TEC consists of the rotor, rotor hub, nacelle, tripod and the tower which joins the nacelle body to the tripod. The TEC is mounted on the seabed using the piled tripod with the rotor hub positioned 18 m above the seabed. The rotor diameter (D) is 18 m. During slack water, the nacelle is rotated about the tower axis so that the rotor faces the dominant flow direction during both ebb and flood tides. The turbine has a cut-in speed of 1 m/s, rated speed of 2.7 m/s and a cut-off speed of 3.4 m/s. Table 1 summarises the specifications of the DeepGen-IV turbine.

Table 1. Specifications of the DeepGen-IV tidal turbine.

TEC Characteristics	Units	Values
Hub height	m	18
Rotor diameter	m	18
Cut-in speed	m/s	1
Rated speed	m/s	2.7
Cut-off speed	m/s	3.4
Rated power	MW	1

Figure 1. The CAD model of the 1 MW DeepGen-IV tidal turbine (**left**) and the turbine being deployed from Hatson Quay, Kirkwall, Orkney (**right**).

2.3. Rotor Implementation

The rotor of the 1 MW DeepGen-IV turbine is represented as an actuator disc in TELEMAC-3D, where the rotor thrust is distributed as a momentum source term in the RANS equations over the discretised disc volume. The implementation supports bi-directional tidal operation through separate ebb and flood rotor configurations, each defined with their own orientation angle (θ_{ebb}, θ_{flood}) and hub position, enabling the model to capture the rotor wake in both ebb and flood tides.

The rotor thrust, F_t, is calculated using

$$F_t = \frac{1}{2}\rho\, W\, C_T\, A\, U_{\text{pw}}^2 \tag{6}$$

where A is the rotor swept area, C_T is the thrust coefficient, and U_{pw} is the upstream velocity projected along the hub-height flow direction θ_{hub}, layer-averaged over the sigma layers spanning the rotor. Sigma layers are a terrain-following vertical discretisation bounded by the bathymetry below and the free surface above, with intermediate layers distributed between them. W is an empirical correction factor applied to the thrust coefficient to compensate for blade physics not resolved by the actuator disc RANS formulation at the present mesh resolution for regional-scale applications. It can be calibrated against high-fidelity CFD or field measurements to improve wake deficit prediction at specific downstream distances of interest, with the understanding that a value tuned for near- or mid-wake agreement at measurement locations does not guarantee physical fidelity of the wake at all downstream distances. In this study, W is set to 1 (i.e., no correction applied) to isolate the effect of representing the turbine support structures. The upstream reference velocity is sampled $3D$ (54 m) upstream of the rotor plane centre along the nacelle axis at the current yaw angle θ_{TEC}. This distance lies well outside the near-induction region of the rotor and remains representative of the local inflow. To avoid repeated mesh searches during the simulation, the triangular element containing the upstream sampling point is pre-mapped at initialisation for each integer degree of yaw from -180° to $+180^\circ$. At each time step, the appropriate pre-mapped element is retrieved based on the current θ_{TEC}. Within this element, the horizontal velocity field is reconstructed at the sampling point by barycentric interpolation from the three vertex nodes on each sigma layer, before layer-averaging over the layers spanning the rotor.

The thrust coefficient C_T and power coefficient C_P are evaluated as piecewise cubic functions of the relative inflow velocity, U_{rel}, defined as the component of U_{pw} projected along the rotor axis to account for any yaw misalignment between the flow direction and the rotor normal:

$$U_{\text{rel}} = \left| U_{\text{pw}} \cos(\theta_{\text{hub}} - \theta_{\text{TEC}}) \right| \tag{7}$$

A constant region of the C_T curve is set to 0.82 between 1.0 m/s and 2.7 m/s based on prior CFD simulations [26], while between 2.7 m/s and 3.4 m/s the standardised C_T curve from [27] is adopted. Below the cut-in speed (1.0 m/s) and above the cut-out speed (3.4 m/s), C_T is set to zero and no rotor thrust is applied. The C_P curve is derived by fitting piecewise cubic segments to the measured power curve published in [28], and the instantaneous power output is computed as

$$P = \frac{1}{2} \rho \, C_P \, A \, U_{\text{rel}}^3 \tag{8}$$

It should be noted that the thrust force calculation (Equation (6)) uses U_{pw}^2, whereas C_T is evaluated at U_{rel} (Equation (7)) and the power output (Equation (8)) uses U_{rel}^3. Classical actuator disc theory evaluates both power and thrust with axial velocity while the applied thrust here uses U_{pw}^2, consistent with the convention applied to the support structures at the same upstream sampling point (Section 2.4). The C_T and C_P curves of the DeepGen-IV turbine used in this study are presented in Figure 2.

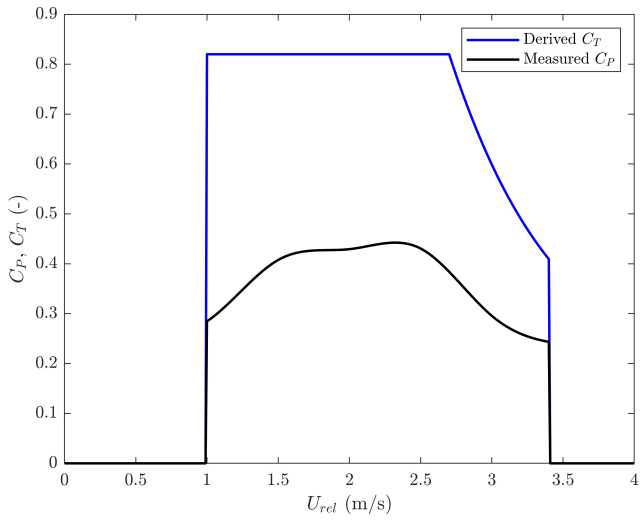

Figure 2. The derived thrust coefficient and measured power coefficient curve of the 1 MW DeepGen-IV tidal turbine.

To account for the thrust exerted by the disc on the surrounding flow, a volumetric source term, S_i, is added to the RANS momentum equations at the computational nodes enclosed by the rotor disc:

$$S_i = \frac{F_t}{V_{\text{element}} \cdot \rho} \tag{9}$$

in units of m/s^2, where V_{element} is the discretised volume of the rotor as represented in the computational mesh. The density ρ in the denominator cancels with ρ in F_t (Equation (6)), so the implementation computes $S_i = \frac{1}{2} W \, C_T \, A \, U_{\text{pw}}^2 / V_{\text{element}}$ directly. The use of V_{element} rather than the idealised geometric volume (i.e., the product of disc thickness and swept area) is important because it reflects the true volume over which the source term is distributed, accounting for the irregular prismatic elements of the unstructured mesh. The dis-

cretised volume is recomputed at each time step with appropriate partition weights applied for parallel domain decomposition.

The rotor disc geometry is dependent on position and orientation. At each time step, a membership test determines whether a computational node lies within the disc volume at its current heading and position by decomposing the displacement vector from the rotor centre into along-axis and perpendicular components in a coordinate frame aligned with θ_{TEC}. A node is classified as inside the rotor disc if

$$|s_{\mathrm{along}}| \leq \tfrac{1}{2}\, t_{\mathrm{disc}} \quad \text{and} \quad t_{\mathrm{perp}}^2 + \Delta z^2 \leq R^2 \tag{10}$$

where s_{along} and t_{perp} are the along-axis and perpendicular distances between the computational node and the rotor plane centre, t_{disc} is the disc thickness (set to 1.7 m in this study), Δz is the vertical distance from the rotor plane centre, and R is the rotor radius. This formulation represents the rotor as a discretised circular disc, ensuring that the momentum source terms are applied only to nodes geometrically enclosed by the disc at its current position and orientation. The vertical extent of the rotor is defined by prescribed sigma layer indices (L_1, L_2) specified in the configuration file.

Figure 3 summarises the implementation of the rotor and support structure source terms in TELEMAC-3D.

2.4. Support Structure Implementation

The tripod, tower, and nacelle are represented as permeable drag volumes, with momentum source terms applied to account for their hydrodynamic influence on the surrounding flow. This avoids the mesh complexity and numerical instability that would arise from embedding fully solid geometries directly within the regional unstructured mesh. Source terms are applied at nodes flagged within the prescribed structural volumes.

The drag source term for a support structure is expressed as

$$S_d = \frac{\frac{1}{2} C_d\, A_f\, U_{\mathrm{s}}^2}{V_{\mathrm{element}}} \tag{11}$$

where C_d is the drag coefficient, A_f is the frontal area of the structure projected normal to the inflow, U_{s} is the upstream velocity magnitude, and V_{element} is the discretised volume of the structure in the computational mesh. As with the rotor source term (Equation (9)), the density ρ cancels between the numerator and the implied division by ρ.

The upstream reference velocity for each support structure is evaluated at the same sampling point used for the rotor (i.e., $3D$ upstream along the nacelle axis at the current yaw angle θ_{TEC}), but layer-averaged over the sigma layers spanned by the respective structure rather than the rotor layers. This convention is methodologically consistent with the standard drag coefficient definition, in which C_d is referenced to the undisturbed approach flow ahead of the structure rather than to the locally disturbed flow at the structure itself. The drag force is applied as horizontal x- and y-source term components opposing the flow direction, distributed uniformly across all flagged nodes within the prescribed volume of the structures so that the integrated force matches the total drag.

Equation (11) uses U_{s} together with a fixed frontal area. This is exact for the cylindrical tower, justified for the nacelle by its rotation with the rotor in each tidal state, and an approximation for the tripod whose triangular planform presents an incidence-dependent projected area. For the present geometry and the ebb and flood axes (320.8° and 137.1°), the projected frontal widths in the two tidal states are 17.30 m and 17.26 m respectively (a 0.2% difference), and the corresponding projected frontal areas differ by the same fraction. A single fixed frontal area of 45 m^2 is therefore used for both tidal states (Table 2).

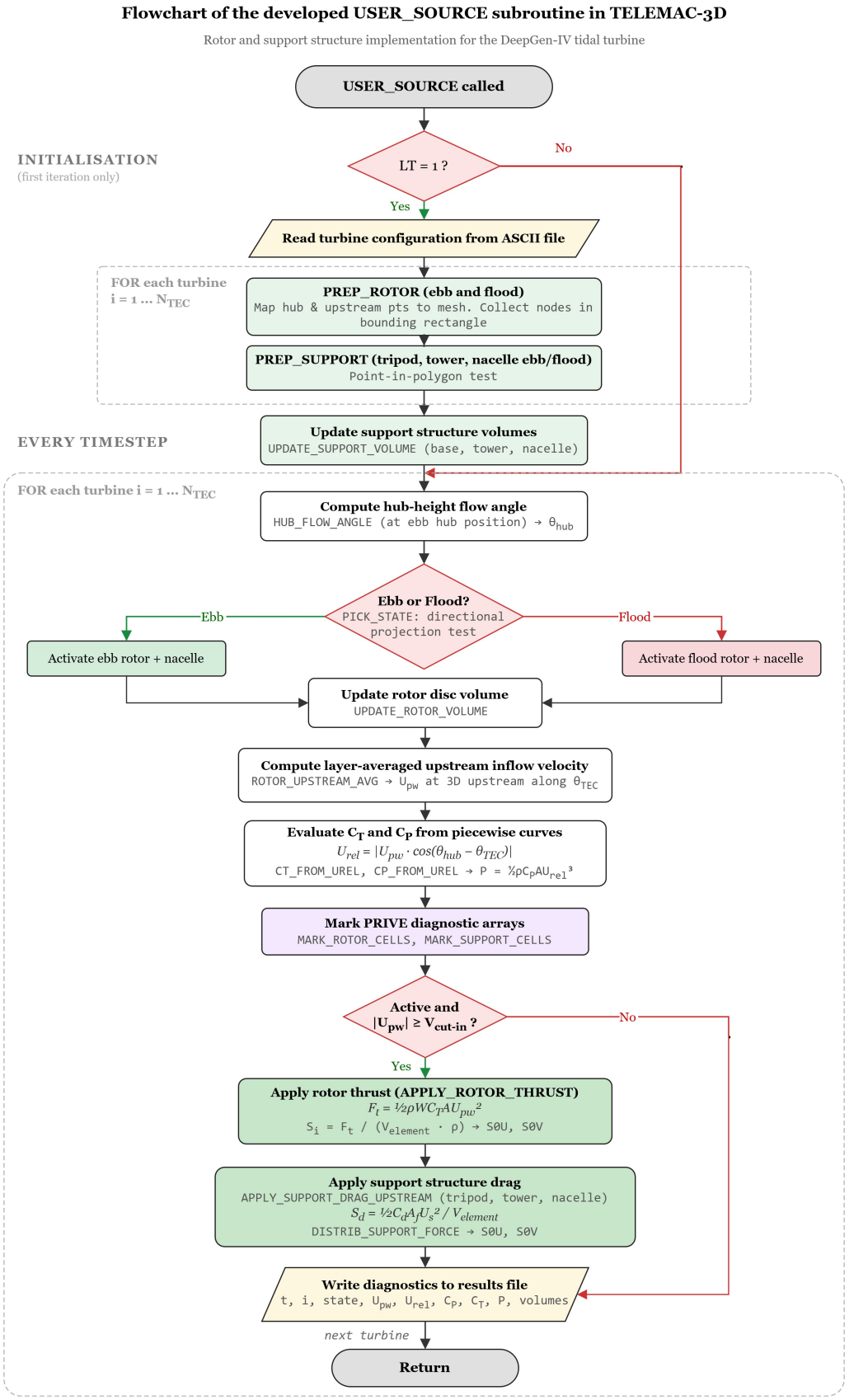

Figure 3. Summarised flowchart of the rotor and support structure implementation in the `USER_SOURCE` subroutine in TELEMAC-3D.

Table 2 summarises the support structure characteristics adopted for the DeepGen-IV turbine at the Fall of Warness, based on public-domain information and engineering estimates where required. The drag coefficients of 0.75, 1.05, and 0.90 for the tripod, tower, and nacelle, respectively, were selected with reference to studies on tripod support structures of offshore wind turbines [29,30], recommended practice for load assessment on marine structures (DNV-RP-C205) [31], and experimental measurements of drag coefficients for circular cylinders in axial flow across a range of length-to-diameter ratios [32].

Table 2. Support structure characteristics of the DeepGen-IV tidal turbine deployed at the Fall of Warness. Nominal dimensions are taken from the turbine CAD model. Tower and nacelle frontal areas are direct geometric projections. The tripod frontal area is the projected area of the simplified triangular-prism representation described in Section 2.4.

Support Structure	Frontal Area	Nominal Dimensions	C_d (–)
Tripod	45 m^2 (approx.)	Height = 8.7 m Distance between piles = 17.3 m Diameter of legs = 0.9 m Diameter of central tower = 2 m	0.75
Tower	14.85 m^2	Diameter = 2 m Height = 7.4 m	1.05
Nacelle	15.9 m^2	Length = 18.8 m Diameter = 3.75 m	0.9

Each support structure is defined by a two-dimensional polygon and a set of sigma layers specifying its vertical extent. The tripod is simplified as a vertical triangular prism whose extrusion height is chosen to preserve the estimated 45 m^2 frontal area of the real structure at a base width of 17.3 m. The tower and nacelle are represented as rectangular prisms based on their nominal dimensions. In the regional sigma layer mesh, the discretised volume of each component varies with the instantaneous water depth over the tidal cycle. Diagnostic outputs from the validation simulation described in Sections 2.5 and 2.6 show that the discretised volumes vary by approximately $\pm$3.6% for the tower and nacelle and $\pm$6.5% for the tripod about their mean values over the four-day validation window. The integrated drag force applied by each structure is invariant under this variation because the frontal area is prescribed from the structure geometry rather than computed from the discretised volume. The variation therefore affects only the local source term magnitude within the structure volume and not the total momentum sink applied to the flow.

Separate nacelle representations are defined for ebb and flood conditions. At each time step, only the nacelle associated with the active tidal state is activated, ensuring that nacelle drag is applied on the physically correct side of the rotor in each flow direction.

The implementation supports multiple turbines within a single simulation domain through a shared ASCII configuration file, although only a single device is evaluated here. Diagnostic outputs—including instantaneous values of upstream velocity, relative velocity, C_T, C_P, power, and discretised volumes for each turbine component—are written to a results file at prescribed intervals for post-processing and validation.

Figure 4 illustrates the rotor and support structure representations on an idealised channel mesh, highlighting the flagged nodes associated with each component and confirming that the intended disc and structural volumes are resolved correctly. The implementation approach is applied to the regional-scale model of the Fall of Warness, with the turbine placement and ebb/flood rotor configurations presented in Section 2.5.

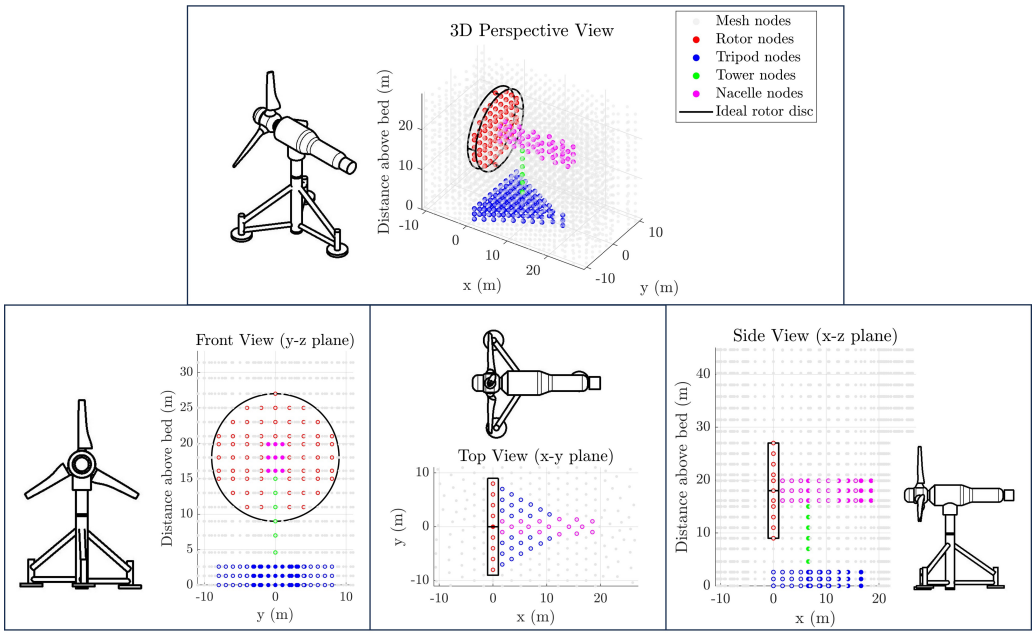

Figure 4. Rotor and support structure representation of the DeepGen-IV turbine with computational nodes overlaid, shown in an idealised rectangular channel domain with uniform depth and fixed horizontal layers to illustrate the representation and implementation. Nodes within each component volume are flagged and colour-coded: rotor (red), tripod (blue), tower (green), and nacelle (magenta). The ideal rotor disc outline is shown in black. Views are presented from the 3D perspective (**top**), front in the *y*–*z* plane (**bottom left**), top in the *x*–*y* plane (**bottom centre**), and side in the *x*–*z* plane (**bottom right**). Schematic renderings of the turbine are included alongside each view for reference.

2.5. Setup of the Regional-Scale Hydrodynamic Model

The regional-scale hydrodynamic model uses the same computational domain as [33], encompassing the Orkney islands and the north coast of mainland Scotland (Figure 5), with an enlarged domain to reduce any boundary effects in the study area. Bathymetry at the Fall of Warness (FoW) was obtained from the UK Hydrographic Office Seabed Mapping Service [34] at 3 m resolution, while EMODnet digital bathymetry [35] at 115 m resolution was used elsewhere in the wider domain. The FoW tidal channel, situated between the islands of Eday and Muckle Green Holm (Figure 5), is characterised by strong tidal flows with ebb tides directed approximately toward the northwest and flood tides toward the southeast. The DeepGen-IV turbine is located at approximately 44 m water depth within the channel.

Three seabed-mounted ADCPs deployed during the ReDAPT project are used for model validation (Table 3; Figure 5). During ebb tides, ADCP01 and ADCP02 lie downstream of the turbine and ADCP03 provides the upstream reference; during flood tides this arrangement reverses. This configuration enables validation of the ambient flow in both tidal directions and wake validation during ebb, when the downstream instruments lie within the core wake region. Data measured at the ADCP01 and ADCP02 locations are available at https://doi.org/10.7488/ds/3448. Full information regarding the series of ADCP and TEC deployments over the measurement campaign period at the FoW tidal test site can be found in [36,37], while the methods for data filtering and quality control can be found in [1].

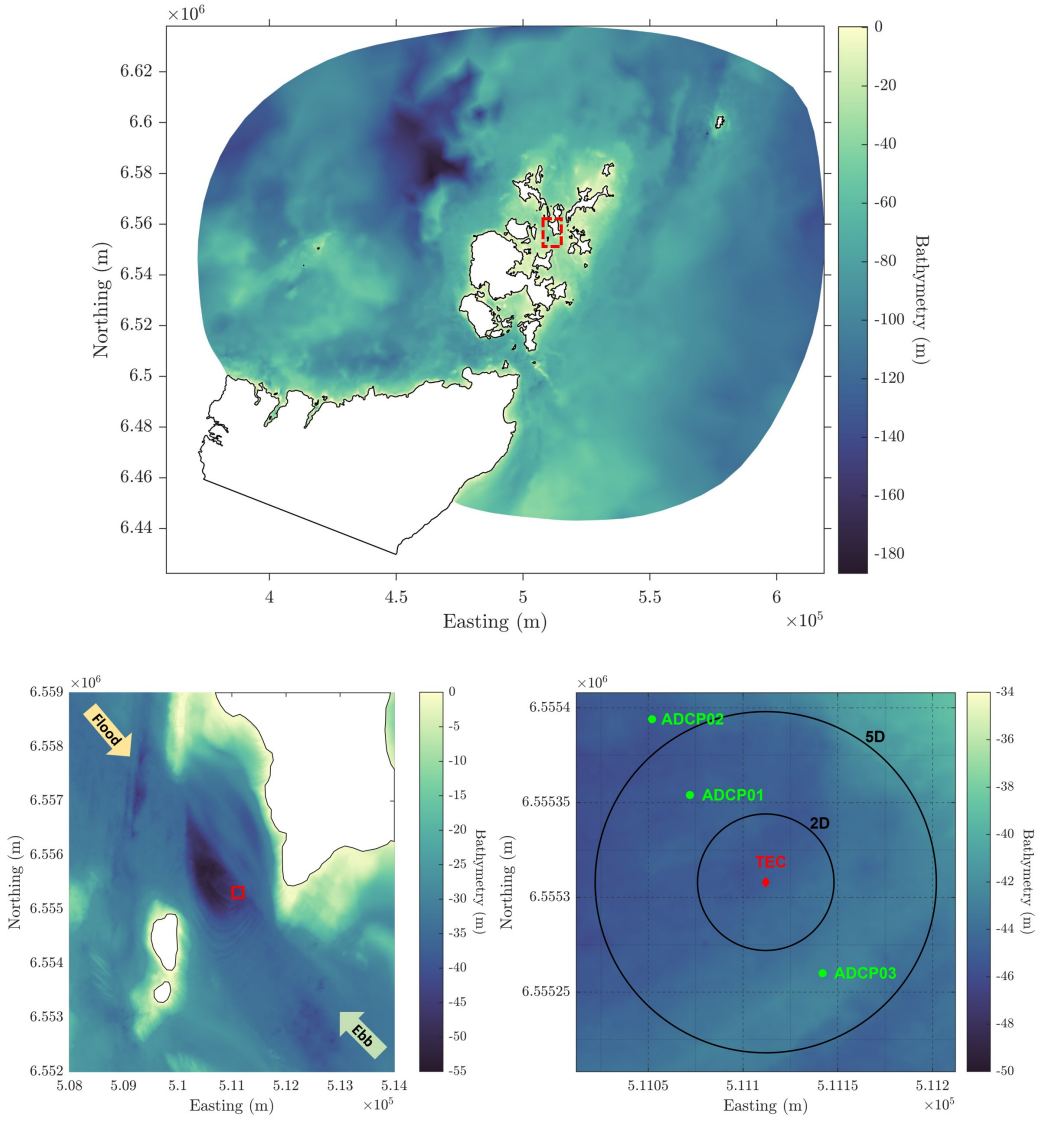

Figure 5. Bathymetry of the regional-scale model domain. (**Top**): Overview of the full computational domain, with coastlines highlighted in black and the Fall of Warness study area indicated by the red dashed rectangle. (**Bottom left**): Zoomed view of the Fall of Warness tidal channel between the islands of Eday and Muckle Green Holm, showing the approximate ebb and flood tidal directions. Red solid rectangle indicates the locations of the instruments. (**Bottom right**): Near-field view centred on the turbine, showing the positions of three seabed-mounted ADCPs (ADCP01, ADCP02, ADCP03) deployed for measurements. Coordinate reference system is WGS84/UTM30N (EPSG:32630).

Table 3. ID, deployment duration and coordinates of the ADCPs involved in the model validation. Distance from rotor plane in turbine diameters for respective ADCPs during the ebb tide are shown. Coordinate reference system is WGS84/UTM30N (EPSG:32630).

ID	Campaign ID	Deployed	Recovered	Days	Easting (m)	Northing (m)	Distance from Rotor Plane in D
ADCP01	ADCP01_NW_Dep5	22 June 2014	5 August 2014	41	511072	6555354	3.7D
ADCP02	ADCP02_NW_Dep5	7 July 2014	16 August 2014	40	511052	6555394	6.2D
ADCP03	ADCP03_SE_Dep5	7 July 2014	17 August 2014	41	511142	6555260	2.8D

The computational domain is discretised using an unstructured triangular mesh with progressive refinement from the open boundaries toward the coastlines and regions of interest, as shown in Figure 6. The mesh resolution ranges from approximately 10 km at the open boundaries to 1.5 m in the immediate vicinity of the turbine, yielding a total of

4,095,960 nodes and 7,640,370 elements (Table 4). The vertical dimension is discretised using 24 sigma layers distributed between the seabed and the free surface, providing sufficient vertical resolution to represent the rotor disc, support structures, and wake development throughout the water column.

Within the FoW region, the mesh is refined to approximately 20 m resolution (Figure 6, bottom left) to resolve the eddies shed downstream of Muckle Green Holm and the shear layer that develops along the northeastern side of the channel, both of which influence the flow structures experienced by the turbine during ebb and flood tides. A very-high-resolution zone is additionally embedded around the turbine, extending approximately 1300 m upstream and downstream along the principal tidal axis during the simulation period to capture the wake in both ebb and flood directions, with a cross-stream width of approximately 10D at the furthest extent (Figure 6, bottom right). Within this zone, the mesh resolution is 1.5 m in the immediate vicinity of the turbine, covering the rotor disc and support structures, and coarsens progressively outward to 7 m at the outer edges. The 1.5 m resolution was selected to place one row of computational nodes across the rotor disc thickness and to resolve the principal dimensions of the support structures, while keeping the overall computational cost manageable. The 7 m outer-edge resolution was informed by a separate mesh sensitivity study in an idealised rectangular channel, ensuring that the wake region is adequately resolved while the gradual coarsening downstream accommodates the expanding wake without additional computational cost.

Open-boundary forcing is imposed using tidal elevation and volume flux from the OSU TPXO tidal atlas [38]. Horizontal turbulence is represented using the k–ε model and vertical turbulence using the Nezu and Nakagawa mixing-length model [23]. Bottom friction is specified using a global Nikuradse roughness length of 0.15 m. The model is run in non-hydrostatic mode, with tidal flats enabled, a time step of 1 s, and output every 60 s for the full domain and every 1 s at instrument locations. A summary of the model configuration parameters is presented in Table 4.

Table 4. Configuration parameters of the regional-scale TELEMAC-3D model.

Parameter	Value
Number of nodes	4,095,960
Number of elements	7,640,370
Number of layers	24
Mesh resolution	1.5–10 km
Coordinate reference system	WGS84/UTM Z30N
Open boundary forcing	Elevation + Volume flux
Horizontal turbulence	k–ε
Vertical turbulence	Mixing-length model (N&N)
Bottom friction	Nikuradse
Roughness length	0.15 (global)
Tidal flats	Yes
Non-hydrostatic	Yes
Simulation time step	1 s
Written time step	60 s (with 1 s output at instrument locations)

The turbine representation in the present study extends the actuator-disc-only approach used in [33], in which only the rotor thrust was modelled without accounting for the drag of the support structures. In the present work, a physics-based representation of both the rotor and the individual support structure components is implemented, as described in Sections 2.3 and 2.4, enabling the relative contribution of each structural component to the overall wake deficit to be quantified independently.

Figure 7 shows the ebb and flood turbine representations on the regional mesh, including the shift in rotor and nacelle position between tidal states. The tripod and tower remain fixed in both directions.

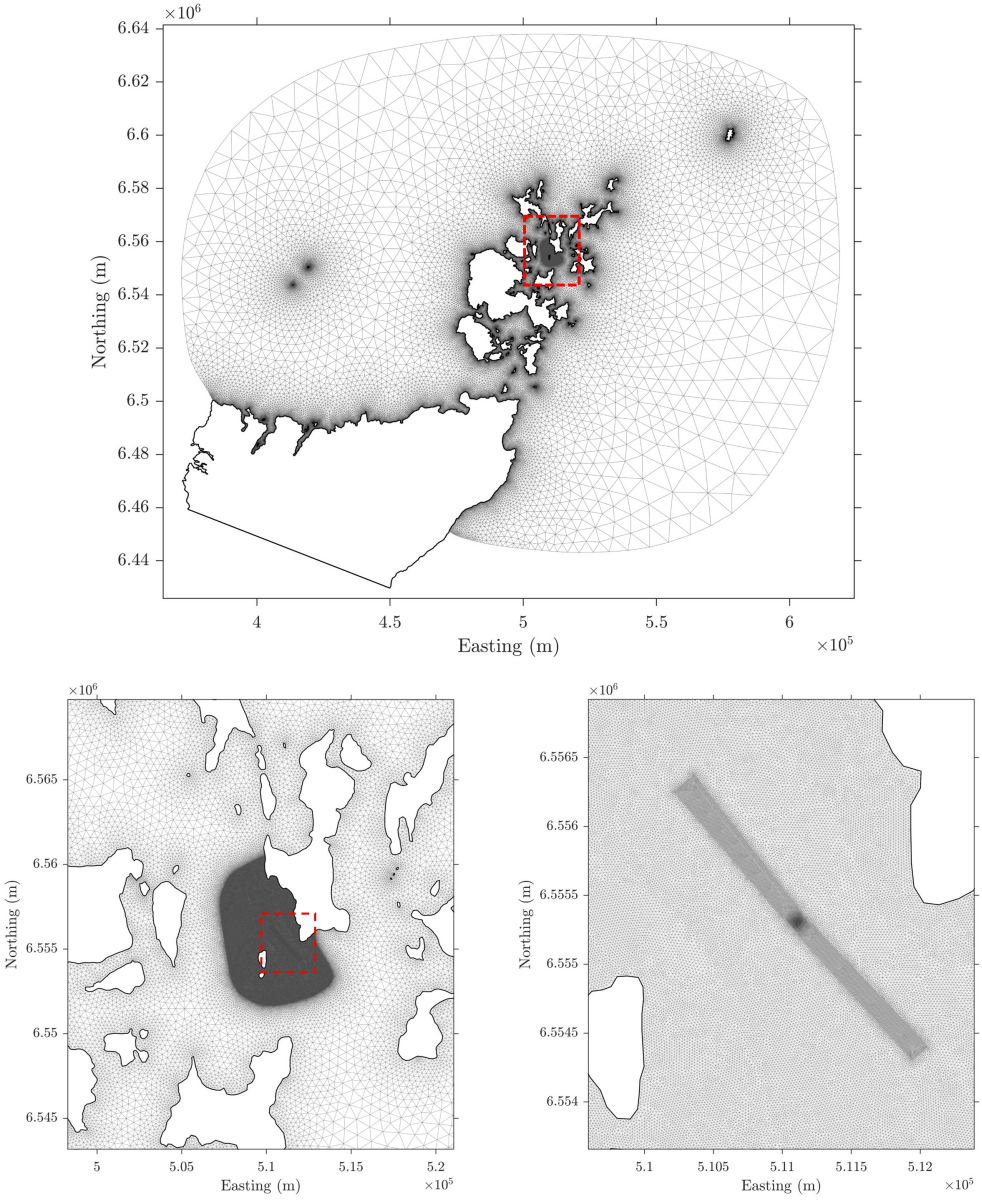

Figure 6. Unstructured triangular mesh of the regional-scale TELEMAC-3D model domain shown at three levels of spatial detail with the red dashed rectangles indicating the zoom-in extent. (**Top**): Full computational domain, with progressive mesh refinement from the open boundaries toward the coastlines and tidal channels. (**Bottom left**): Zoomed view around the Fall of Warness, showing an increased mesh density at the tidal site. (**Bottom right**): Near-field view between the islands of Eday and Muckle Green Holm, showing the high-resolution mesh refinement zone aligned with the principal tidal axis to resolve the turbine wake in both ebb and flood directions. Coordinate reference system is WGS84/UTM30N (EPSG:32630).

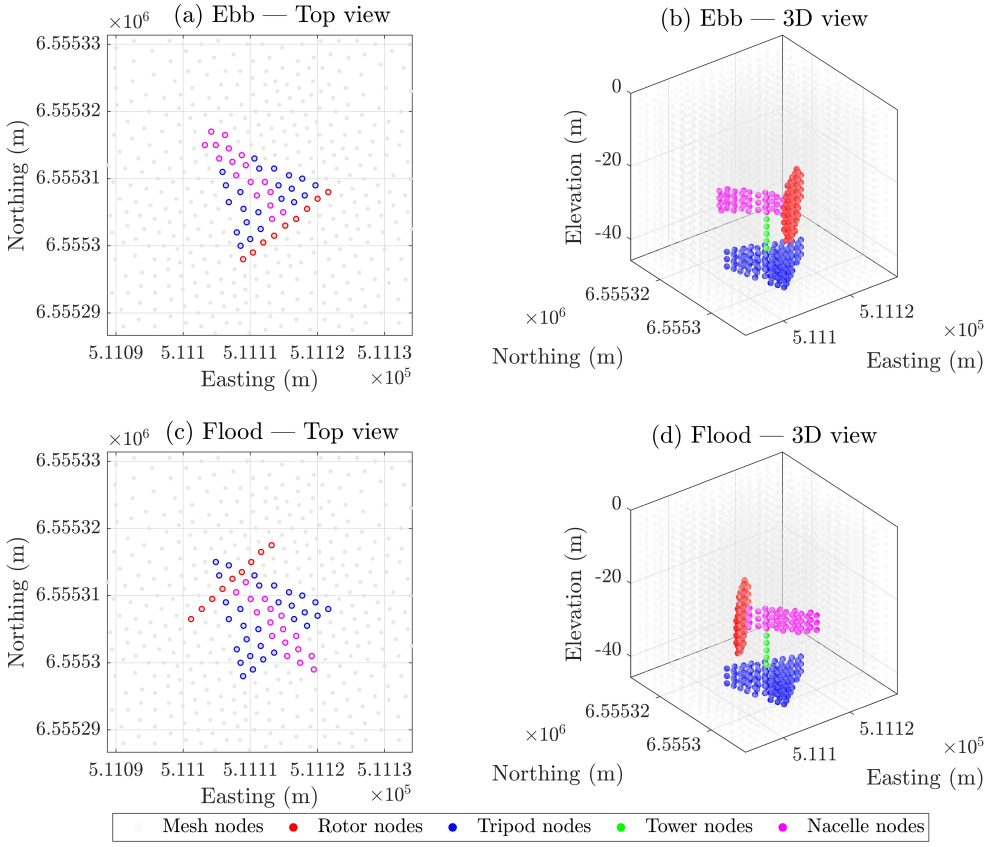

Figure 7. Rotor and support structure representation of the DeepGen-IV turbine in the regional-scale unstructured mesh during ebb (**top row**) and flood (**bottom row**), shown in top view (**left**) and 3D perspective (**right**). Computational nodes flagged within each component volume are colour-coded: rotor (red), tripod (blue), tower (green), and nacelle (magenta). Background mesh nodes within the vicinity of the turbine are shown in light grey. The shift in rotor and nacelle positions between ebb and flood reflects the bi-directional operating configuration, with the nacelle activating on the downstream side of the rotor relative to the incident flow in each tidal state. The tripod and tower positions remain fixed. Elevations are referenced to the mean sea level. Coordinate reference system is WGS84/UTM30N (EPSG:32630).

2.6. Model Validation

Three model cases are used to isolate the incremental effect of support structures on wake prediction: ambient flow without the turbine, rotor-only, and rotor plus support structures. This incremental approach isolates the contribution of the support structures to the overall wake deficit and allows direct comparison of wake characteristics between the rotor-only and rotor-plus-structures cases against ADCP field measurements. A validation period of 16 July 2014 to 20 July 2014 is adopted, covering four days selected for the availability of measured wake data during turbine operation, and minimal wave activities at the site, with the mean significant wave height during this period less than 0.8 m. The window sits within the broader spring-neap variability captured by the ADCP measurements at the site (22 June to 17 August 2014; see [33], Figure 8a). The model was spun up over a 24 h period on 2014-07-15 prior to the validation period using initial conditions generated from the tidal atlas data, sufficient for initial condition transients to dissipate at the study site before the validation window. All simulations were performed on the ARCHER2 UK National Supercomputing Service using 8 nodes (1024 cores), requiring approximately 3.5 to 4 h of wall-clock time per simulation day.

Validation is conducted in two stages and limited to ebb tides. First, the ambient flow field is assessed against upstream ADCP measurements using velocity profiles and hub-layer time series. Second, the wake predictions from the rotor-only and rotor-plus-structures cases are compared with measured downstream wake profiles during ebb tides, when ADCP01 and ADCP02 lie within the wake region. During flood tides, ADCP03 is downstream of the turbine but its position relative to the flood-tide wake trajectory places it outside the wake core, so flood validation is not supported by the deployment. As the wake trajectory varies over each tidal half-cycle, the modelled wake does not continuously pass over the downstream ADCPs. Following the approach in [33], only time steps for which the modelled wake centreline intersects the ADCP locations are retained. At each output time step, the angle between the line from the rotor centre to the hub-height wake centreline and the line from the rotor centre to each ADCP location is computed. Samples are retained where the angular difference is within $\pm 2^{\circ}$, evaluated at the corresponding downstream distance of $3.7D$ for ADCP01 and $6.2D$ for ADCP02. This ensures that the retained samples represent instances when the modelled wake core is passing over the instrument location, enabling a consistent comparison between measured wake profiles and modelled wake-core conditions.

3. Results

3.1. Model Predictions of Ambient Flow at Upstream Locations

Ambient flow performance is assessed by comparing modelled velocities with ADCP measurements at the upstream reference locations for each tidal state.

Figure 8 presents time-series comparisons of the hub-height velocity magnitude (distance above the seabed (z) = 18 m) at the three upstream ADCP locations over the four-day validation period. Data are highlighted by whether the measured velocity is above or below the turbine cut-in speed of 1.0 m/s. Good agreement between modelled and measured velocity is observed throughout the flood periods at ADCP01 and ADCP02, and during the ebb periods at ADCP03, with R^2 values of 0.954, 0.949 and 0.944 respectively. The model captures the tidal asymmetry between successive half-cycles and reproduces the peak velocities of each tidal phase. Larger discrepancies are observed during slack tide transitions when the velocity falls below 1.0 m/s. Since the wake validation is restricted to upstream velocities between the cut-in and rated speeds (1.0 to 2.7 m/s), error metrics are reported both for the full dataset (n) and for the filtered subset (n^*) retaining only samples where the measured and modelled velocity exceeds 1.0 m/s. The filtered RMSE* values are 0.144, 0.160 and 0.212 m/s for ADCP01, ADCP02 and ADCP03 respectively.

The corresponding time-series of hub-height flow direction is shown in Figure 9. During the active flow periods ($U \geq 1.0$ m/s), the modelled flow direction is approximately 130–150° during flood at ADCP01 and ADCP02, and around 310–330° during ebb at ADCP03, in good agreement with the measurements. The unfiltered R^2 values for flow direction are 0.527, 0.465 and 0.700 for ADCP01, ADCP02 and ADCP03 respectively, which are notably lower than those for velocity magnitude. This is largely attributable to the rapid directional variability during slack tide transitions, when the flow speed is small and the direction is poorly defined, which degrades the correlation. The unfiltered RMSE values (22.0°, 22.4° and 11.0° for ADCP01, ADCP02 and ADCP03) similarly reflect this observation during slack tide. After filtering for $U \geq 1.0$ m/s, the RMSE* reduces substantially to 5.15°, 5.77° and 3.55° respectively, confirming that the directional agreement is good during the flow conditions relevant to turbine operation and wake generation.

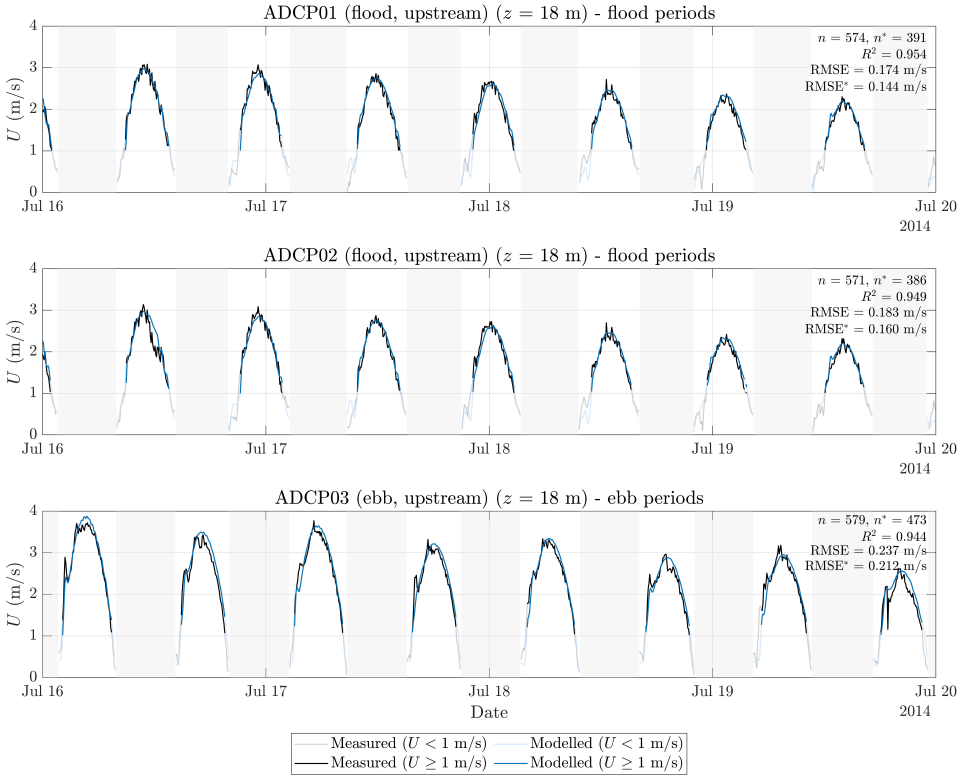

Figure 8. Time-series of hub-height velocity magnitude (z = 18 m) at the three upstream ADCP locations during the validation period (16 July 2014 to 20 July 2014). ADCP01 and ADCP02 are shown during flood periods and ADCP03 during ebb periods. Error metrics are shown for both the full dataset (n, R^2, RMSE) and the filtered subset (n^*, RMSE*) retaining only samples with $U \geq 1.0$ m/s.

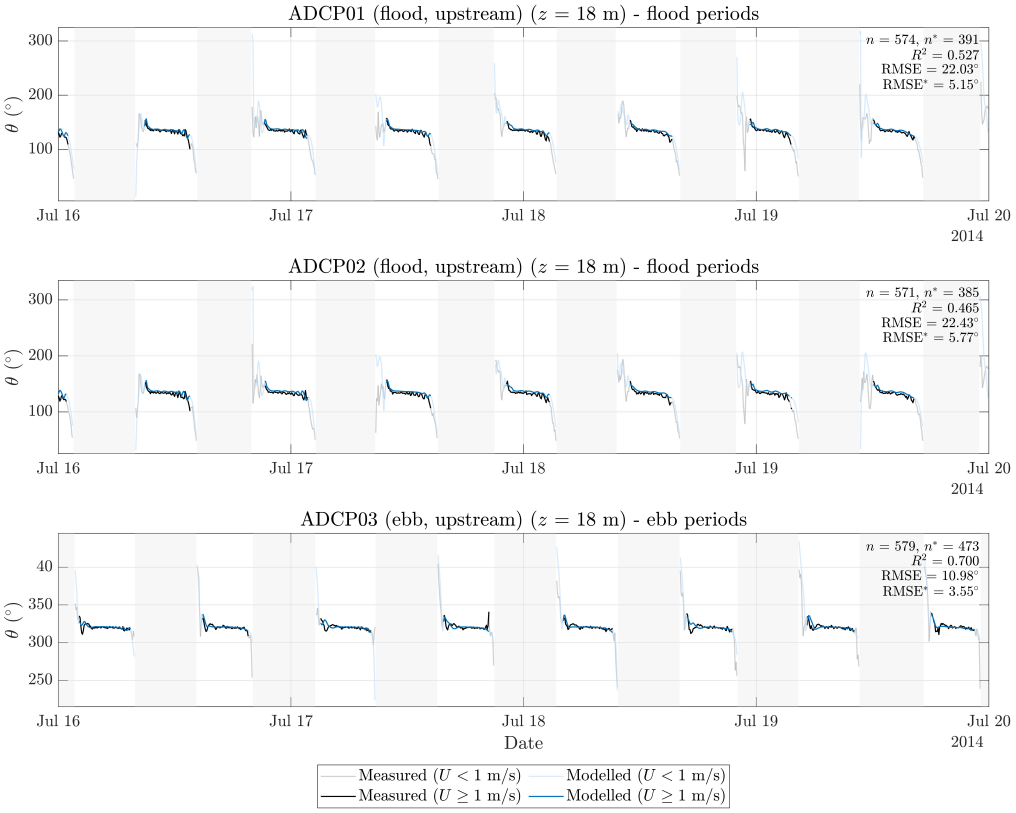

Figure 9. As Figure 8 but for time-series hub-height flow direction.

Figure 10 quantifies the model–measurement agreement through scatter plots of hub-height velocity magnitude and flow direction at the three upstream locations. For velocity magnitude, strong linear correlation is observed at all locations, with R^2 values of 0.954, 0.949 and 0.944 for ADCP01, ADCP02 and ADCP03 respectively. The filtered bias is small and positive at all three locations (0.019, 0.032 and 0.058 m/s), indicating a slight tendency for the model to overestimate the flow speed. The scatter index (SI*) ranges from 0.070 to 0.084, indicating that the root-mean-square error is less than 9% of the mean measured velocity. For flow direction, the filtered RMSE* and MAE* confirm the time-series observations. ADCP03 during ebb shows the tightest directional agreement (RMSE* = 3.55°, MAE* = 2.24°, bias* = 0.45°), while ADCP01 and ADCP02 during flood exhibit slightly larger scatter (RMSE* of 5.15° and 5.77°) with a systematic positive bias of 3.1° and 4.1°, suggesting the model directs the flood flow slightly more toward the south than observed.

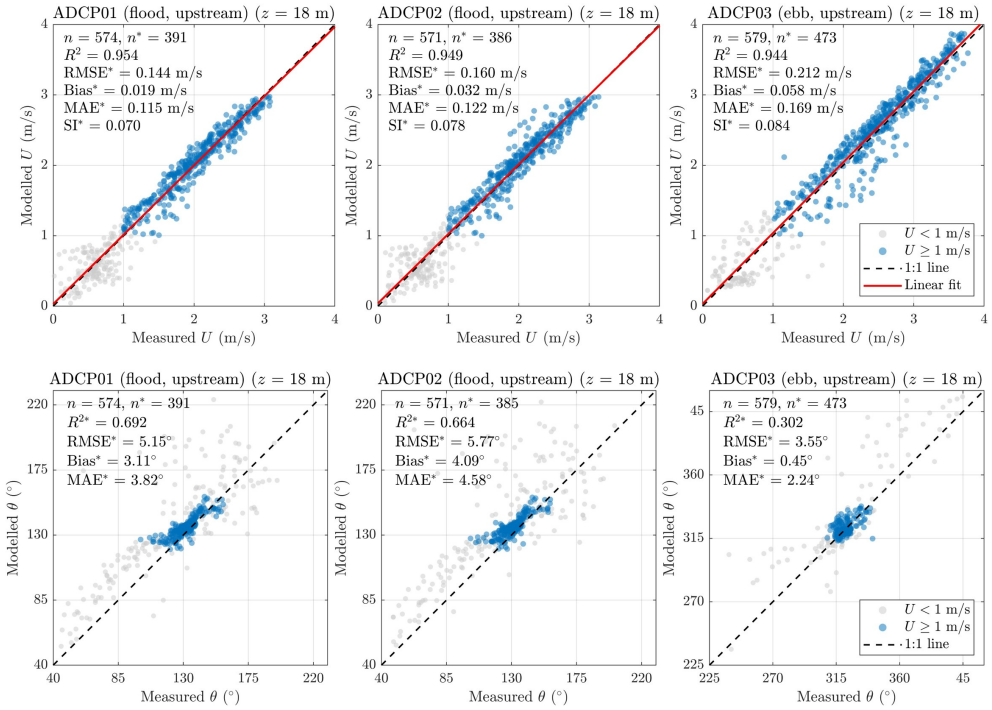

Figure 10. Scatter plots of modelled versus measured hub-height (z = 18 m) velocity magnitude (**top row**) and flow direction (**bottom row**) at the three upstream ADCP locations. Blue points indicate samples with measured $U \geq 1.0$ m/s and grey points indicate $U < 1.0$ m/s. The dashed black line represents the 1:1 line and the red line shows the linear fit. Error metrics annotated with an asterisk (*) are computed using only the filtered subset with $U \geq 1.0$ m/s.

Figure 11 presents the speed-binned velocity profiles at the upstream locations. The mean modelled profiles show good agreement with the measured profiles across all speed bins and throughout the water column at all three locations. Across the speed bins, the mean profiles compare well over the rotor extent, with generally low RMSE values and somewhat larger errors at ADCP03 during the highest ebb-speed bins. This increased error at ADCP03 during higher ebb velocities may be attributed to the stronger shear layer that develops along the northeastern side of the channel at peak ebb flow, which introduces spatial gradients that are sensitive to small differences in the modelled and actual bathymetry.

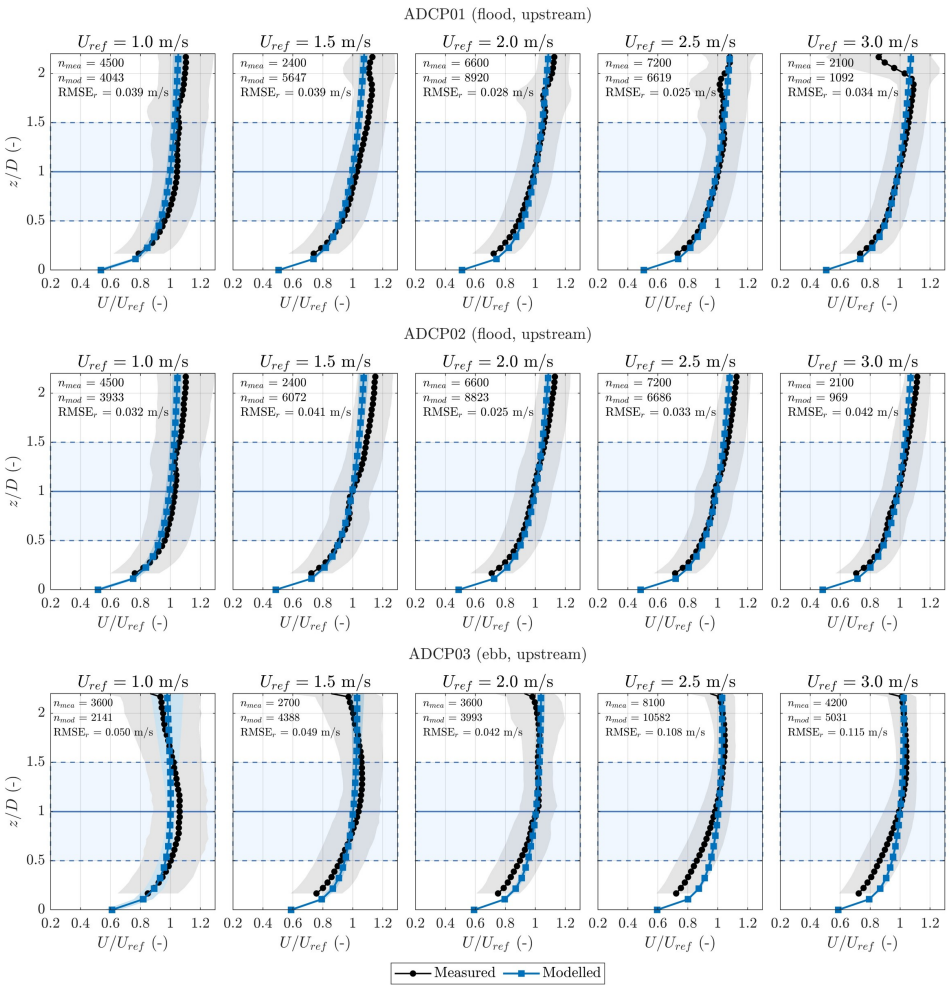

Figure 11. Speed-binned velocity magnitude profiles at the three upstream ADCP locations. Black lines with circular markers show the mean measured profiles and blue lines with square markers show the mean modelled profiles. Shaded regions indicate ± 1 standard deviation of the sample distribution at each vertical level within the corresponding bin, for the measured (grey) and modelled (blue) profiles. Horizontal blue areas and lines indicate the rotor extent, the hub height (z/D = 1.0, solid) and rotor tip positions (z/D = 0.5 and 1.5, dashed). The number of measured (n_{mea}) and modelled (n_{mod}) samples and the RMSE over the rotor extent (RMSE$_r$) are annotated in each panel. Comparison within the top 15% of the water column are excluded due to acoustic side-lobe interference.

Two features of the velocity profile comparison can be observed here. First, the standard deviation of the modelled profiles is noticeably smaller than that of the measured profiles across all speed bins and locations. This is expected given the RANS formulation of the model, which resolves the mean flow and large-scale tidal variability but does not capture the turbulent fluctuations that contribute to the measured variance. Second, there is a tendency for the modelled profiles to diverge from the measurements toward the top of the water column, particularly above z/D = 2.0. This is partly attributable to the absence of wind- and wave-driven surface effects in the model, and partly to the increased measurement uncertainty associated with acoustic side-lobe interference in the upper bins of the upward-looking ADCPs. Although the upper 15% of the water column has been excluded from the measured profiles due to acoustic side-lobe interference, the remaining bins near this boundary may still be affected by reduced measurement accuracy as the beam spread widens toward the free surface. The absence of wind- and wave-driven surface effects in the model may also contribute to this divergence, as wave-induced orbital velocities and wind-driven shear would modify the velocity profile in the upper water column.

3.2. Comparison of Modelled and Measured Wake Profiles

The wake predictions from the rotor-only and rotor-plus-structures cases are compared against measured velocity profiles at the two downstream ADCP locations during ebb tides. Both the modelled and measured velocity profiles are at 1 Hz temporal resolution. Velocity magnitude at each location is normalised by the reference upstream hub velocity (U_{ref}) probed at the ADCP03 location. The filtered profiles are grouped into six speed bins from 1.5 to 2.5 m/s at 0.2 m/s intervals with a bandgap of ± 0.05 m/s. The normalised error between modelled and measured profiles, $(U_{\text{mod}} - U_{\text{mea}})/U_{\text{ref}}$, is also presented to quantify the improvement of including support structures. The percentage change in RMSE between the rotor plus structures and rotor-only cases is reported over both the water column between 3 and 27 m above the seabed, $0.17 \leq z/D \leq 1.5$, (ΔRMSE_c) and the rotor extent, $0.5 \leq z/D \leq 1.5$, (ΔRMSE_r), where positive values indicate that the rotor-plus-structures case achieves a lower RMSE than the rotor-only case.

Figure 12 presents the wake velocity profiles at ADCP01, located $3.7D$ downstream of the rotor plane. Both model cases underpredict the velocity deficit relative to the measurements across all speed bins, as indicated by the modelled profiles being shifted toward higher U/U_{ref} values compared to the measured profiles. However, the rotor-plus-structures case consistently produces a deeper wake deficit than the rotor-only case, bringing the modelled profiles closer to the measurements. This is clearly visible within the rotor extent, where the additional drag from the support structures reduces the velocity through the wake core. The improvement is quantified in the lower panels. ΔRMSE_r is positive across all six speed bins, ranging from 6% at U_{ref} = 1.7 and 2.1 m/s to 15% at U_{ref} = 1.9 m/s. ΔRMSE_c is similarly positive across all bins, ranging from 9% to 18%, with an average improvement of approximately 14%.

The velocity deficit at hub height (z/D = 1.0) increases with U_{ref} for both model cases and the measurements, consistent with the increasing thrust applied by the rotor at higher flow speeds. Across all speed bins, the rotor-plus-structures case reproduces the measured hub-height deficit more closely than the rotor-only case. Below the rotor extent ($z/D < 0.5$), the rotor-plus-structures profiles show additional velocity reduction compared to the rotor-only case across all speed bins. This is attributable to the drag of the tripod and tower, which occupy this region of the water column and is only represented in the rotor-plus-structures case. The presence of this additional deficit below the rotor is a distinguishing feature of the support structure representation and contributes to the improved agreement with the measured profiles.

Figure 13 presents the corresponding comparison at ADCP02, located $6.2D$ downstream. At this further downstream location, the wake has partially recovered and the velocity deficit is less pronounced than at ADCP01 for both the measurements and the model predictions. The rotor-only and rotor-plus-structures profiles are closer together than at ADCP01, indicating that the influence of the support structures on the modelled wake profile diminishes with downstream distance as flow mixing acts to homogenise the wake. Nevertheless, the rotor-plus-structures case still provides an improvement over the rotor-only case for the majority of speed bins, with ΔRMSE_c values of 11%, 37%, 4%, 9% and 3% at U_{ref} = 1.7, 1.9, 2.1, 2.3 and 2.5 m/s respectively. The exception is at U_{ref} = 1.5 m/s, where ΔRMSE_c is -10%. However, the modelled sample sizes at this speed bin are very small (n_R = 43, n_{R+S} = 44), making this comparison less statistically robust.

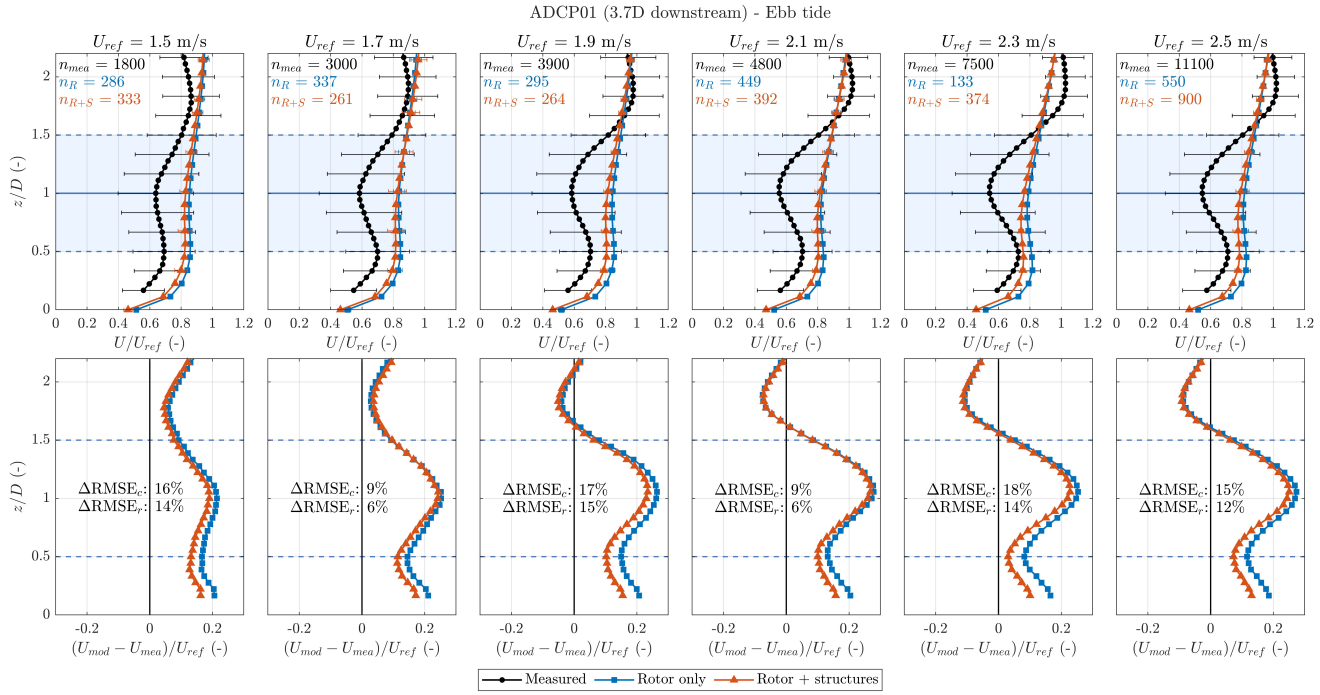

Figure 12. Comparison of modelled and measured velocity magnitude profiles in the wake at the location of ADCP01 (3.7D downstream) during ebb tides. (**Top row**): Normalised velocity magnitude profiles at six reference upstream velocity bins. Black lines with circular markers show the mean measured profiles with ±1 standard deviation error bars (as defined in Figure 11), blue lines with square markers show the rotor-only case, and orange lines with triangular markers show the rotor plus structures case. (**Bottom row**): Normalised error between modelled and measured profiles. ΔRMSE_c and ΔRMSE_r indicate the percentage improvement in RMSE from the rotor-plus-structures case over the rotor-only case, evaluated over $0.17 \leq z/D \leq 1.5$ and the rotor extent respectively. The number of measured (n_{mea}), rotor-only (n_R) and rotor-plus-structures (n_{R+S}) samples are annotated in each panel. Comparison within the top 15% of the water column are excluded due to acoustic side-lobe interference.

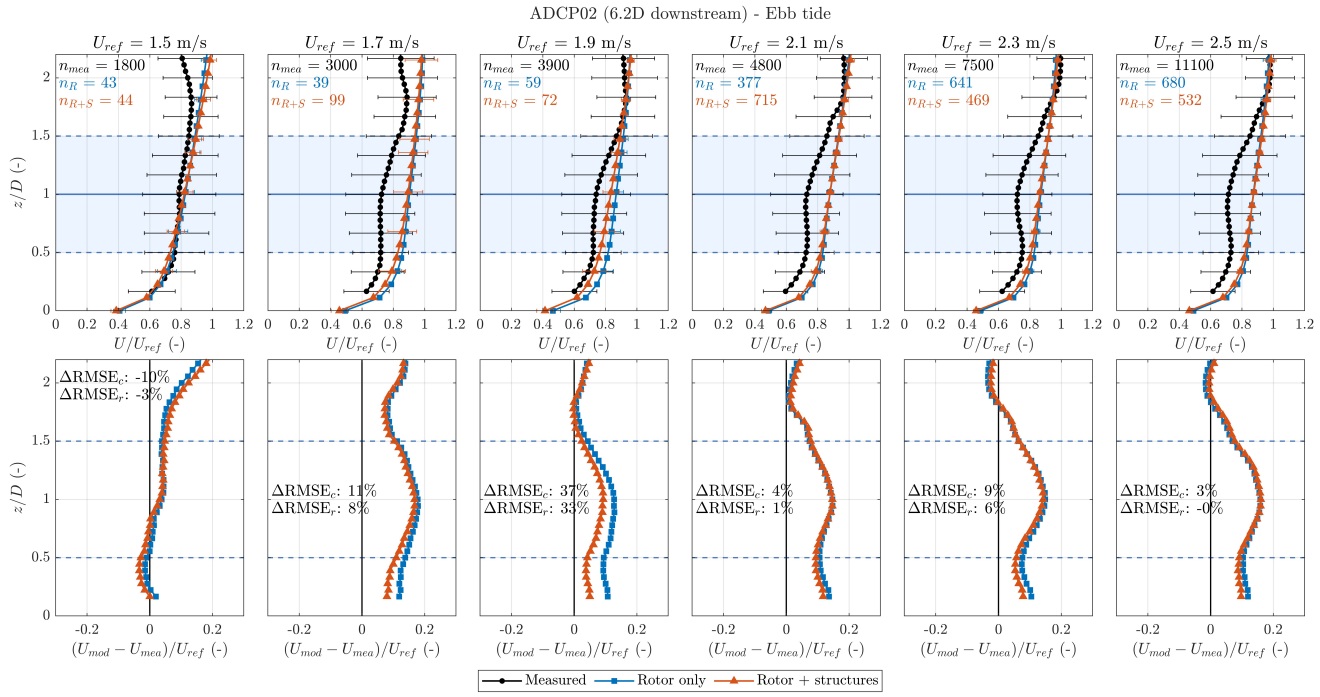

Figure 13. As Figure 12 but at the location of ADCP02 (6.2D downstream) during ebb tides.

The tripod-induced deficit observed at ADCP01 is also visible at ADCP02, although less pronounced. The rotor-plus-structures profiles continue to show lower velocities below z/D = 0.5 compared to the rotor-only case. The sample sizes for the two model cases (n_R and n_{R+S}) differ at several speed bins, particularly at ADCP02 where the rotor-only case yields notably fewer filtered samples at lower speeds (e.g., n_R = 43 and n_{R+S} = 44 at 1.5 m/s; n_R = 39 and n_{R+S} = 99 at 1.7 m/s). This arises from a combination of geometric and flow-related effects. ADCP01 and ADCP02 are not co-linear with the rotor plane centre, so the wake centreline filter selects different subsets of time steps for each instrument even within a single case. Between cases, the modelled wake trajectory itself differs slightly through two mechanisms: the structural drag deflects the wake position directly, and the perturbation it imposes on the surrounding flow field accumulates over the simulation, producing a phase mismatch in the eddy structures that displaces the modelled wake at the ADCP locations. The RMSE comparison at ADCP02 at individual speed bins should therefore be interpreted as indicative rather than strictly controlled, since the two cases are not evaluated against an identical set of wake-core time steps. The aggregate cross-bin improvement nonetheless remains a robust qualitative indicator, with the rotor-plus-structures case retaining a deeper wake deficit below the rotor hub, consistent with the better-sampled ADCP01 comparison.

As observed in the ambient and upstream flow validation, the standard deviation of the modelled wake profiles is smaller than that of the measurements across all speed bins and both locations. This discrepancy is more pronounced in the wake than in the upstream flow, as turbulent fluctuations are amplified by the shear layers bounding the wake and the turbulence generated by the support structures, neither of which is fully resolved by the RANS formulation.

3.3. Influence of Support Structure Representation on Wake Deficit and Recovery

Having established in the previous section that the rotor-plus-structures case improves the agreement with measured velocity profiles at both downstream ADCP locations, the analysis in this section is now focused on the broader spatial characteristics of the wake and how the support structures modify its extent and recovery.

3.3.1. Hub-Height Velocity Deficit Fields

Figures 14 and 15 present the hub-height velocity deficit fields for the rotor-only and rotor-plus-structures cases during ebb and flood tides respectively, at three reference upstream velocities (U_{ref} = 1.5, 2.0 and 2.5 m/s). Each panel is a snapshot extracted from a single ebb half-cycle on 16 July 2014 and a single flood half-cycle on 18 July 2014, selected at the time step when the upstream reference velocity corresponds to each speed bin. The deficit is defined as the percentage reduction in velocity magnitude relative to the no-turbine (ambient flow) case at each node and time step. In both tidal states and across all flow speeds, including the support structures produces a longer wake. The 5% deficit contour, which is a metric of practical interest to turbine and array developers for determining minimum spacing requirements, extends noticeably further downstream in the rotor-plus-structures case.

The near-field insets show that the rotor-plus-structures wake is stronger in the immediate vicinity of the turbine, with the 2D planforms of the structure representations overlaid. Beyond the core wake regions, both ebb and flood fields exhibit patches of positive and negative deficit in the ambient flow, particularly during flood tide. These features arise in part from slight phase mismatches in the eddy structures between the ambient flow and turbine simulations. The presence of the turbine subtly modifies the surrounding flow field, causing eddies shed from the local coastline or bathymetry to evolve on slightly

different trajectories, which produces localised apparent deficit or acceleration when the two fields are compared at the same instant. Despite this contamination in the ambient field, the wake itself is clearly distinguishable and the effect of the support structures on its extent is consistent across both tidal states.

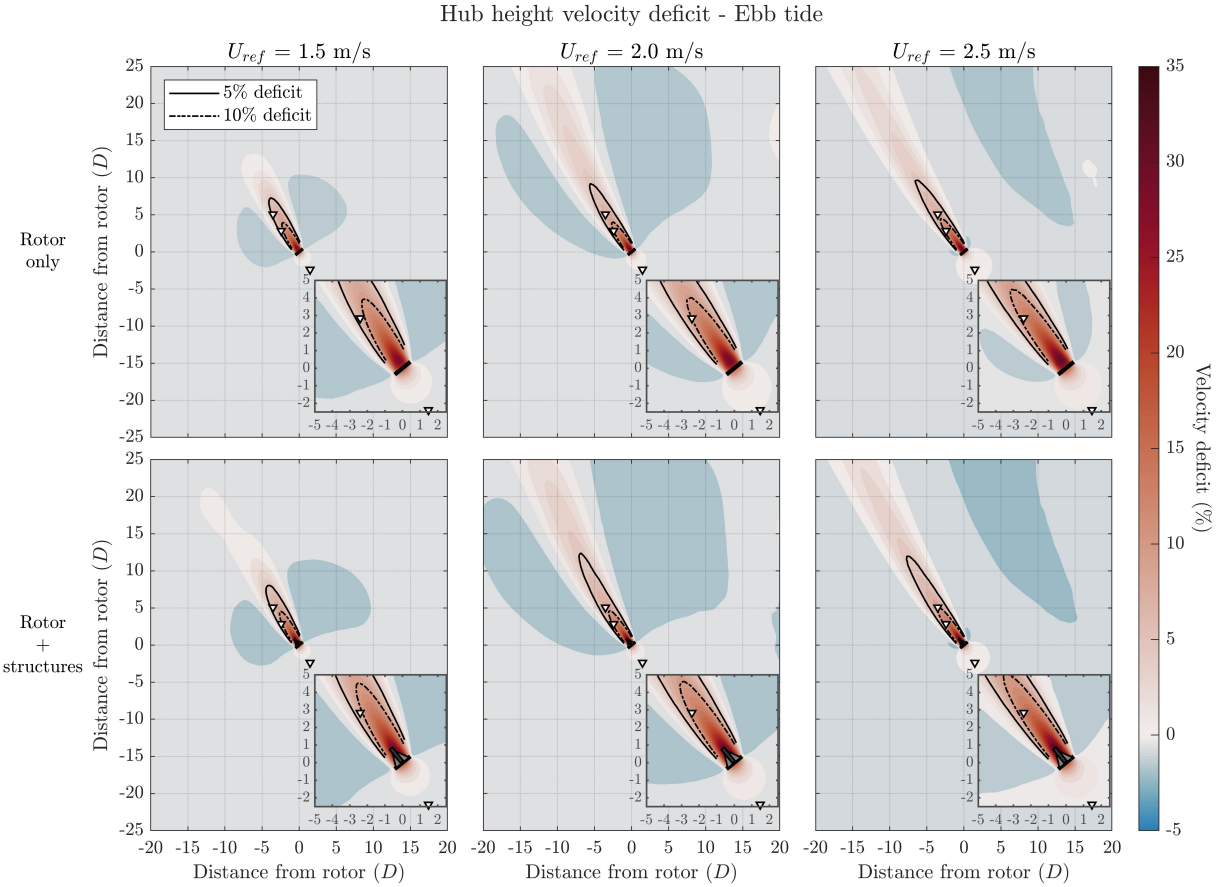

Figure 14. Hub-height velocity deficit fields during ebb tides for the rotor-only (**top row**) and rotor-plus-structures (**bottom row**) cases at three reference upstream velocities (U_{ref} = 1.5, 2.0 and 2.5 m/s). Solid and dash-dotted contours indicate the 5% and 10% velocity deficit levels respectively. Locations of the three ADCPs are indicated by the arrowhead markers. Inset panels show the near-field wake structure within 5D of the rotor plane. 2D planforms of the rotor and structure representations are overlaid. Easting and northing are normalised by D with the rotor plane centre as the origin and the underlying coordinate reference system is WGS84/UTM30N (EPSG:32630).

3.3.2. Centreline Deficit Decay and Wake Extent

The along-wake evolution of the deficit is quantified in Figure 16, which tracks the hub-height velocity deficit along the wake centre as a function of downstream distance (1–25D) for the same snapshots shown in Figures 14 and 15. At each downstream increment of 0.25D, the centreline is defined by the lateral position of the peak deficit, allowing the curve to follow the wake trajectory rather than a fixed axis perpendicular from the rotor plane. At all three reference velocities and in both tidal states, the rotor-plus-structures case maintains a higher centreline deficit than the rotor-only case, with the largest separation occurring within the first 5D downstream where the structure drag increases the deficit by approximately 2–8%. Beyond 5D, the gap between the two cases narrows but a persistent offset remains out to 25D. During ebb at 2.0 and 2.5 m/s, both cases retain a deficit of 3–5% at 25D, with the rotor-plus-structures case consistently 1–2% higher than the rotor-only case. At U_{ref} = 1.5 m/s during ebb, the rotor-only deficit decays to near zero by about 15D, while the rotor-plus-structures case retains a residual deficit of 2–3% to the end of the domain.

During flood, the deficit decay follows a broadly similar pattern, although the curves retain a higher residual deficit of 3–5% at 25D compared with the ebb case. At U_{ref} = 1.5 m/s, the flood deficit curves are noticeably separated, though this likely reflects differences in the ambient flow field between the simulation cases rather than a proportionally larger wake effect at this speed.

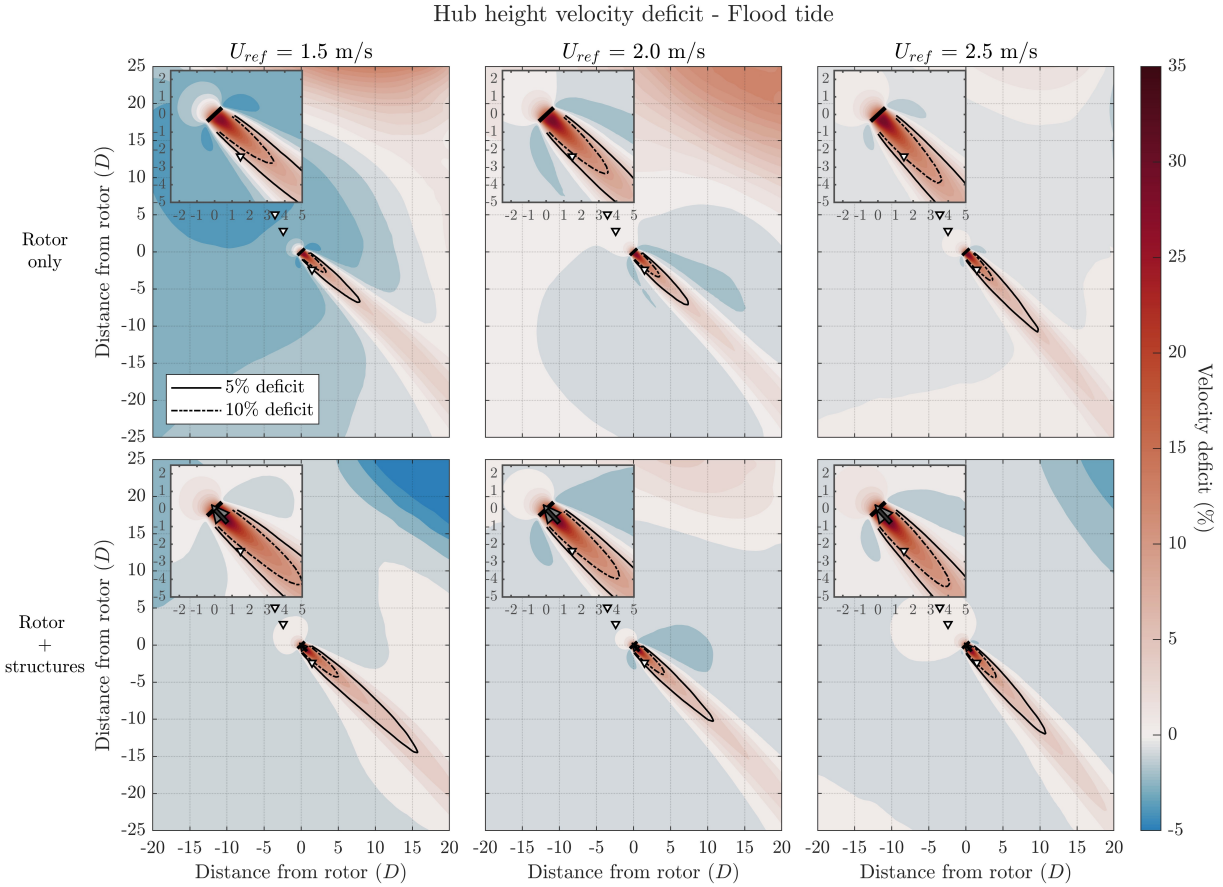

Figure 15. As Figure 14 but during flood tides.

To characterise the downstream extent of the wake more precisely, Figure 17 reports the distance at which the hub-height centreline deficit falls below 5% ($D_{5\%}$) from U_{ref} = 1.3 to 3.1 m/s, covering the operational range of flow speeds encountered during the simulation period. The ebb results are extracted from single half-cycle snapshots on 16 July 2014, as the high temporal and spatial flow variability at the Fall of Warness during ebb tides—driven by eddies shed from the surrounding coastline and bathymetry, which evolve on slightly different trajectories between the ambient flow and turbine simulations due to the turbine influence on the surrounding flow field—produces far-field velocity differences between the simulation cases that are comparable in magnitude to the wake deficit itself, making ensemble-based wake extent quantification less robust. The ebb $D_{5\%}$ values are therefore illustrative of the specific flow conditions of the chosen half-cycle and should not be interpreted as ensemble-representative statistics in the same sense as the flood values. During flood tides, ambient flow is more spatially uniform with less eddy activity near the northeastern coast, allowing an ensemble approach. The flood results are therefore presented as ensemble medians computed over all valid snapshots across the speed bins throughout the simulation period, with interquartile range (IQR) bands reflecting the variability in wake extent at each speed bin (±0.05 m/s).

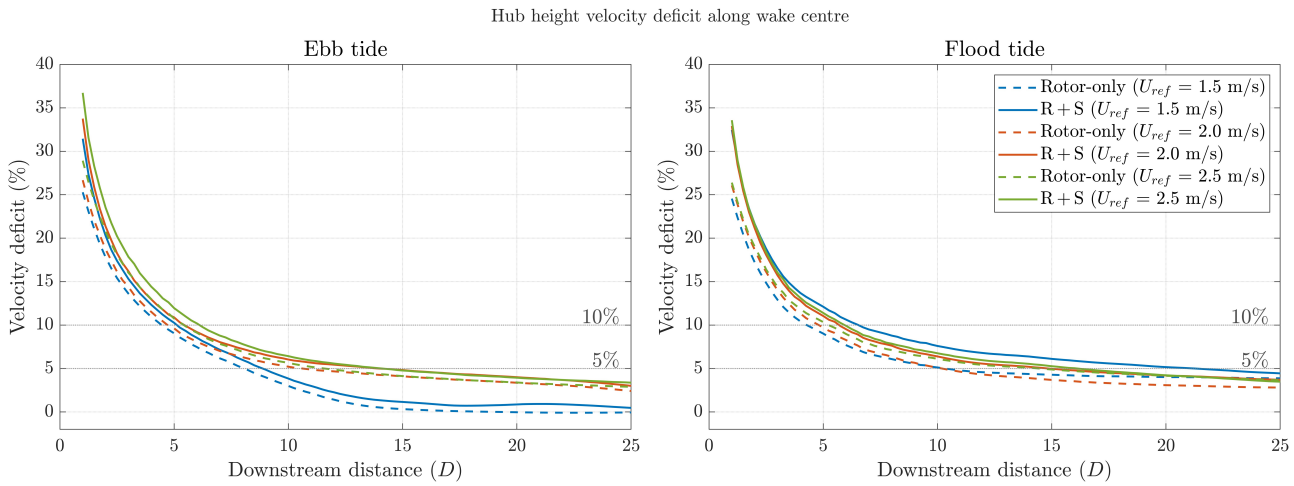

Figure 16. Hub-height velocity deficit along the wake centreline as a function of downstream distance from 1 to 25D during ebb (**left**) and flood (**right**) tides. Dashed lines indicate the rotor-only case and solid lines indicate the rotor-plus-structures (R + S) case.

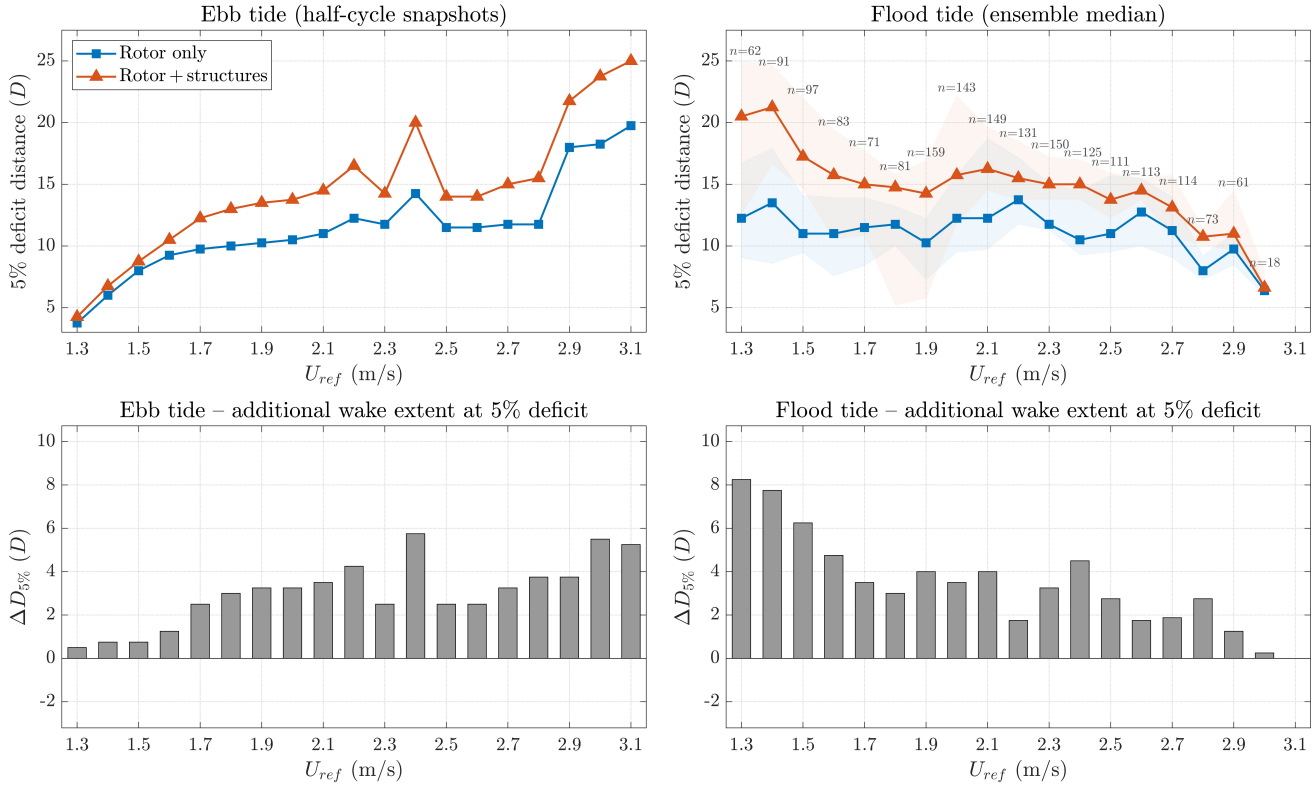

Figure 17. (Top row): Downstream distance at which the hub-height centreline velocity deficit falls below 5% ($D_{5\%}$) as a function of reference upstream velocity during ebb ((**left**), half-cycle snapshots) and flood ((**right**), ensemble median with interquartile range bands). (**Bottom row**): Additional wake extent attributable to the support structures, $\Delta D_{5\%} = D_{5\%,\mathrm{R+S}} - D_{5\%,\mathrm{R}}$, during ebb (**left**) and flood (**right**). The number of ensemble samples (n) is annotated at each speed bin for the flood tide.

During the ebb tide, $D_{5\%}$ generally increases with flow speed for both model cases. Below U_{ref} = 1.5 m/s, both cases produce short wakes of 4–8D with minimal separation, consistent with the low rotor thrust near cut-in speed. Above 1.5 m/s, the rotor-plus-structures case yields a progressively longer wake, with $\Delta D_{5\%}$ growing from approximately 1D at 1.5 m/s to 3–6D at higher speeds. The wake extent continues to increase above rated speed (2.7 m/s), reaching approximately 20D for the rotor-only case and 25D for the rotor-

plus-structures case at 3.1 m/s. Since these values are each extracted from a single snapshot at a specific instant within the tidal half-cycle, some scatter is expected as the wake extent at any given moment depends on the instantaneous flow conditions, which vary continuously through the tidal cycle.

During flood tides, the ensemble median of $D_{5\%}$ for the rotor-plus-structures case ranges from 7 to 20D across the speed bins, generally exceeding the rotor-only values by 2–6D in the operational range between 1.5 and 2.5 m/s. The IQR bands are wide for both model cases, spanning 3–5D at most speed bins. This spread reflects both the variability in wake extent across the ensemble and the sensitivity of the 5% threshold to the instantaneous differences in ambient flow between the simulation cases, which vary from snapshot to snapshot. At the lowest speeds (1.3–1.5 m/s), the flood $D_{5\%}$ values are notably higher than the ebb values, which likely reflects the influence of the ambient flow variability on the deficit calculation rather than a physical wake effect, as the wake signal is weak at these speeds. Above 2.7 m/s, the flood sample sizes decrease sharply (n = 73, 61 and 18 at 2.8, 2.9 and 3.0 m/s respectively), and the two model cases converge. The additional wake extent attributable to the support structures, $\Delta D_{5\%}$, averages approximately 3D (∼54 m) across both tides within the operational speed range of 1.5 to 2.5 m/s. For array layout design, this implies that a rotor-only wake model would underestimate the downstream distance required for wake recovery, potentially leading to overly compact turbine spacing.

3.3.3. Wake Structure Through the Water Column

The vertical and lateral structure of the wake is examined through spanwise transect cross-sections at 1D, 3.7D and 6.2D downstream of the rotor plane. Figures 18 and 19 present these transects for ebb and flood tides respectively, extracted from the same snapshots as the U_{ref} = 2.5 m/s panels in Figures 14 and 15. The lateral distance from the hub is expressed in rotor diameters (D), with negative values corresponding to the left side of the wake when looking downstream and positive values to the right.

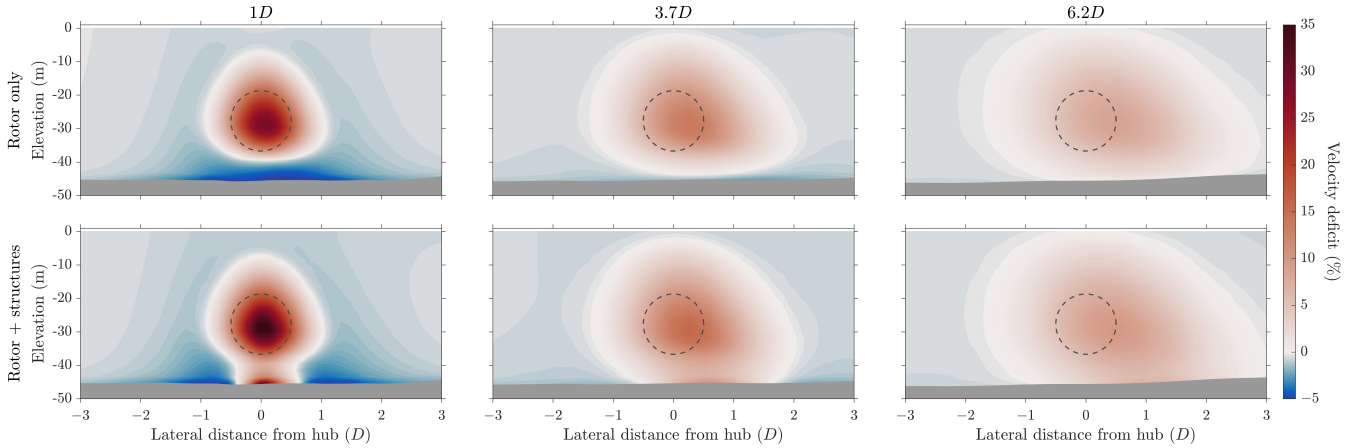

Figure 18. Spanwise transect cross-sections of velocity magnitude deficit at 1D, 3.7D and 6.2D downstream of the rotor plane during the ebb tide at U_{ref} = 2.5 m/s. (**Top row**): Rotor-only case. (**Bottom row**): Rotor-plus-structures case. The dashed circle indicates the projected rotor swept area. Grey shading denotes the seabed. Lateral distance from the hub is expressed in D, with negative values to the left and positive values to the right when looking downstream. The underlying coordinate reference system is WGS84/UTM30N (EPSG:32630). Elevation is referenced to mean sea level.

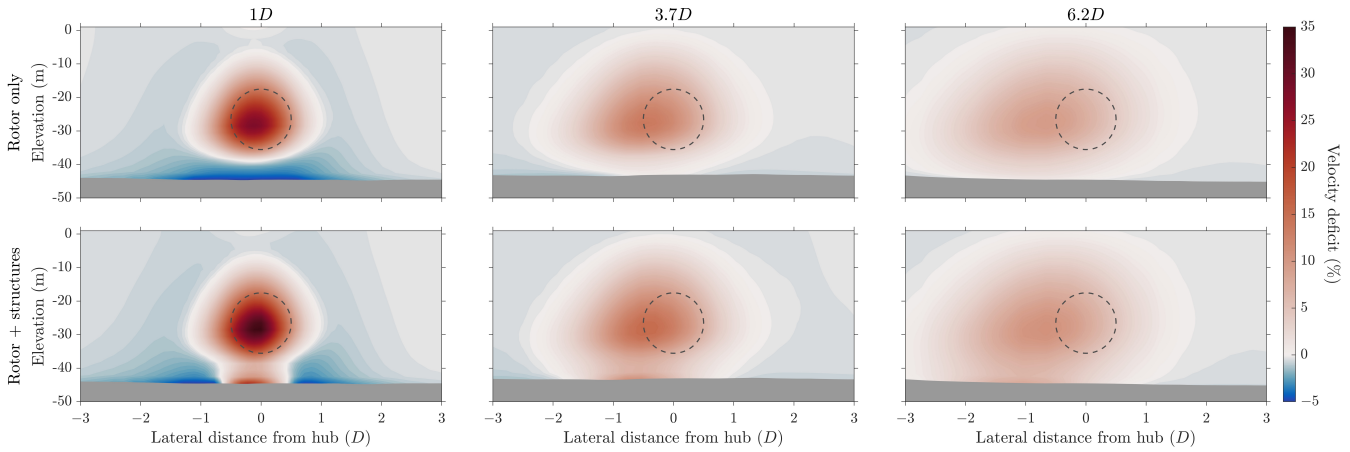

Figure 19. As Figure 18 but during the flood tide.

At 1D downstream, the rotor-only wake appears as a deficit region centred on the rotor disc, with peak values exceeding 30% and the wake already spreading laterally beyond the swept area. The rotor-plus-structures case produces a stronger deficit exceeding 35%, with the highest values concentrated around the hub where the nacelle drag augments the rotor-induced deficit. A region of flow acceleration (negative deficit) is visible near the seabed in both model cases, more prominently in the rotor-only case. The rotor-plus-structures case shows pronounced additional deficit below the rotor extending toward the seabed, directly attributable to the tripod and tower drag which is absent from the rotor-only simulation. By 3.7D, the overall deficit has diminished and the wake has spread further laterally. The rotor-plus-structures case continues to exhibit deeper deficit in the lower water column, though the vertical asymmetry is less pronounced than at 1D. At 6.2D, the deficit has reduced to 10–15% and the wake is substantially wider than the rotor diameter. The rotor-plus-structures case still produces a visibly deeper deficit than the rotor-only case across the full water column, especially near the seabed. Both ebb and flood transects show a slight lateral asymmetry in the deficit distribution, with the wake core shifted toward the positive lateral direction during ebb and toward the negative direction during flood. This reflects the influence of the ambient flow conditions on the wake trajectory and confirms the observations of the hub-height velocity deficit fields in Figures 14 and 15. The flood tide transects (Figure 19) display a similar progression, with the rotor-plus-structures case producing deeper deficit than the rotor-only case at all three downstream distances. The seabed profile varies across each transect, reflecting the irregular bathymetry at the Fall of Warness, and differs between the ebb and flood as the two sets of transects cut through the seabed at different locations and orientations.

4. Discussion

4.1. Effect of Support Structures on Wake Prediction Performance

The upstream validation shows that the ambient flow is reproduced with sufficient accuracy for wake assessment, so the differences between the rotor-only and rotor-plus-structures cases can be interpreted primarily in terms of turbine representation. Including the support structures improves agreement with measured wake profiles at both downstream ADCP locations, with the clearest improvement at 3.7D downstream.

This improvement arises mainly because the support structures alter the vertical structure of the wake. The rotor-plus-structures case produces additional deficit below the rotor and a stronger deficit near hub height, bringing the predicted profiles closer to the measurements. This is consistent with the added drag from the tripod, tower, and nacelle,

and is supported by the transect analysis showing enhanced deficit, lower water column and greater vertical asymmetry.

Both model cases still underpredict the measured wake deficit, particularly in the near wake. This is consistent with known limitations of actuator disc RANS formulations, which do not resolve blade-scale turbulence or finer near-wake structures at the near-to-mid-wake distances (3.7 and 6.2D) where the ADCPs are located. Another potential contributor is the C_T curve itself. Since site-specific thrust measurements were not available, any C_T mismatch cannot be assessed for this deployment. Since the thrust correction factor was fixed at $W = 1$, the present results should be interpreted primarily as evidence that support structure representation improves wake prediction relative to a rotor-only regional model, rather than as a fully calibrated prediction of wake magnitude.

4.2. Wake Extent and Implications for Array Layout

The centreline deficit and $D_{5\%}$ analyses show that including the support structures increases wake persistence relative to the rotor-only case. For the present turbine and site, the additional wake extent is about 3D on average over the operational flow range, equivalent to roughly 54 m. This means that a rotor-only regional model would underestimate the downstream distance required for recovery to within 5% of the ambient flow.

This difference is relevant across the full range of practical inter-row spacings considered in tidal array design. Reported streamwise spacings between rows range from approximately 2–5D in closely packed staggered configurations to upwards of 40D for full wake recovery [39]. The hub-height 5% wake recovery distances obtained here (5–25D across the operational speed range) lie within this range, so a 3D additional extent attributable to the support structures is non-negligible relative to the spacings at which downstream turbines would typically be placed. However, the exact magnitude should not be treated as generally transferable, as it will depend on turbine geometry, structural drag, and site-specific flow conditions. The more robust conclusion is that support structure drag can materially affect wake recovery predictions in regional-scale models and should therefore be considered when downstream interactions are of interest.

These spacing-relevant findings are obtained from a single turbine, and they quantify the support structure contribution to the wake of one device rather than the cumulative array effects that would inform inter-row spacing decisions in a deployed array. Multi-device simulations using the present support structure representation would address the modification of downstream inflow by upstream wakes, wake–wake interactions as the wakes merge, and the channel-scale blockage and bypass-flow effects that develop as cumulative array thrust increases. These effects can amplify or moderate the single-turbine wake extension reported here, and need to be assessed before the present findings can be translated into specific spacing guidelines for array layout.

The ebb and flood results also show that wake extent estimates are sensitive to ambient flow variability. The structural effect appears clearer in ebb conditions, while flood results are more variable because the deficit calculation is more strongly influenced by differences in the ambient flow field between snapshots.

4.3. Limitations and Sources of Uncertainty

In addition to the limitations of the RANS and actuator disc formulation, several further sources of uncertainty should be acknowledged. The support structures are represented as permeable drag volumes rather than explicit solid geometries, so the tripod, tower, and nacelle are geometrically simplified in ways that preserve frontal area and nominal dimensions but not the exact three-dimensional structure. Features such as the inclination of the tripod piles and the local geometry of pile–pile and pile–tower junctions

are not explicitly resolved. As a consequence, the mean flow distortion produced by the real three-dimensional structures, for example, the time-averaged velocity asymmetries or flow blockage arising from pile inclination, are approximated rather than resolved. Unsteady features such as vortex shedding, unsteady separation, and junction-generated coherent turbulence are not represented, as capturing these features requires both resolved structural geometry and a scale-resolving turbulence approach, neither of which is intended within the present regional-scale formulation. These features predominantly influence the very-near wake within roughly one rotor diameter of the structures, where geometry-resolved CFD with a scale-resolving turbulence approach, for example, Large-Eddy Simulation (LES), would be required to capture them. The present formulation is appropriate for the regional-scale objective of this study, which concerns the integrated effect of structural drag on wake recovery and centreline deficit at distances of 3.7D and beyond. The improved agreement with measured wake profiles at the downstream ADCPs reflects the integrated drag contribution rather than the resolution of specific near-wake flow features.

The validation strategy is also constrained by the ADCP layout. As noted in Section 2.6, ADCP03 lies outside the wake core during flood tides, so a fair comparison between measured and modelled wake profiles is not supported for flood tides. The deficit fields and downstream distance metrics presented for flood tides should accordingly be interpreted as indicative model behaviour rather than directly validated predictions.

The wake centreline filter applied at ADCP01 and ADCP02 is designed to compare measured and modelled profiles only when the modelled wake core passes over each instrument, providing a fair within-case validation against the measured wake. However, the modelled wake trajectory differs between the rotor-only and rotor-plus-structures cases, through the direct deflection imposed by the structural drag and a phase mismatch in the eddy structures of the surrounding flow that accumulates over the simulation as the drag perturbs the wider flow field. The two cases are therefore not evaluated against an identical set of wake-core time steps, and the RMSE comparison particularly at ADCP02 should be interpreted with this in mind. Within the present 4-day simulation window, restricting both cases to a strictly matched set of wake-core time steps is not practical at all speed bins, because the intersection of the two retained sample sets becomes too small at low speeds at ADCP02 for meaningful comparison. Extending the simulation period to average out this trajectory variability, alongside investigation of alternative filter and binning criteria for the wake profile comparisons, are identified as directions for future work.

The drag coefficients assigned to the support structures were taken from published studies of analogous geometries. To bound the response to uncertainty in these values, a component-level sensitivity analysis was performed in an idealised rectangular channel (Appendix A). Perturbing the drag coefficient of each component by $\pm$20% individually changed the hub-height $D_{5\%}$ by less than $\pm$2% (Table A1), confirming the robustness of the qualitative wake-extension finding to plausible C_d uncertainty within the published range. For near-bed structures, the modelled approach velocity depends on the Nikuradse bottom friction parameterisation, which together with the published C_d uncertainty bounds the precise magnitude of the tripod drag contribution. The present results therefore reflect a physically motivated and sensitivity-verified choice of structural drag parameters, although not uniquely calibrated to deployment-specific measurements.

Finally, the velocity deficit calculation is sensitive to small differences in ambient flow features between the turbine and no-turbine simulations. At the Fall of Warness, this is most evident during ebb tides, where differences in the position of eddies and shear structures can contaminate far-wake deficit estimates and limited the wake extent analysis to single half-cycle snapshots. The main conclusion that support structures increase wake persistence remains robust, but the precise magnitude of far-wake metrics should be interpreted with

this uncertainty in mind. The 4-day validation window also samples a limited range of tidal and ambient flow conditions, so the wake extent results should not be treated as fully representative of long-term variability across spring-neap or seasonal timescales.

4.4. Applications and Future Work

The permeable drag volume approach developed here is not specific to the DeepGen-IV tripod configuration. In principle, other bottom-mounted support concepts could be represented by prescribing appropriate planform geometry, vertical extent, frontal area, and drag coefficient, and the same framework could be extended to floating systems by representing relevant hull or mooring-related components as additional drag volumes. The implementation also supports multiple turbines within a single domain, although such applications were not evaluated in the present study.

The results further suggest that support structure effects may be relevant beyond hub-height wake recovery alone. In particular, the extension of the velocity deficit into the lower water column indicates a possible influence on near-bed flow modification, with potential implications for future studies of bed shear stress, sediment transport, or ecological response [40,41]. These effects were not examined here, but the present representation provides a practical basis for investigating them in coupled regional models.

Future work should examine the sensitivity of the wake metrics to the structural drag coefficients in the regional-scale model and extend the analysis to longer simulation periods spanning a wider range of tidal conditions. The multi-device extension required to inform array-spacing guidelines is discussed in Section 4.2. Additional value would also come from further investigation of the interaction between turbine wakes and channel-scale circulation features at energetic sites such as the Fall of Warness.

5. Conclusions

This study introduced a method for representing tidal turbine support structures within TELEMAC-3D and evaluated its influence on wake prediction for the 1 MW DeepGen-IV turbine deployed at the Fall of Warness, Scotland. The tripod foundation, tower, and nacelle were modelled as permeable drag volumes alongside an actuator disc rotor within a high-resolution regional-scale 3D hydrodynamic model.

The model reproduced the ambient flow with sufficient accuracy to support wake assessment, and including the support structures improved agreement with measured wake profiles relative to the rotor-only case. At 3.7D downstream, the rotor-plus-structures case reduced profile RMSE by 6–18% across the assessed speed bins, while at 6.2D downstream the improvement was positive in five of the six bins considered. The improvement was associated with a stronger deficit near hub height and, importantly, additional deficit below the rotor due to drag from the tripod and tower.

Including the support structures also increased wake persistence. Across the operational flow range examined here, the hub-height 5% wake recovery distance increased by about 3D on average, equivalent to approximately 54 m. Transect analysis further showed that the support structures extend the velocity deficit into the lower water column and enhance the vertical asymmetry of the wake, a finding whose implications for near-bed processes such as bed shear stress and sediment transport are not quantified here and are identified as future work.

Taken together, these results indicate that support structure drag can materially affect wake prediction in regional-scale tidal turbine models and should be considered where wake persistence and downstream interactions are important. The implementation is extendable to other support concepts and multi-device studies, although such applications remain to be evaluated.

Author Contributions: Conceptualization, R.L. and B.S.; methodology, R.L. and C.O.; software, R.L.; validation, R.L., N.S., T.T. and B.S.; formal analysis, R.L.; investigation, R.L. and B.S.; resources, N.S. and B.S.; data curation, R.L. and B.S.; writing—original draft preparation, R.L.; writing—review and editing, R.L., N.S. and B.S.; visualisation, R.L.; supervision, B.S.; project administration, R.L. and B.S.; funding acquisition, B.S. All authors have read and agreed to the published version of the manuscript.

Funding: This research received no external funding.

Data Availability Statement: The ADCP measurement data used in this study are publicly archived at https://doi.org/10.7488/ds/3448. The simulation output files, configuration files, and the custom TELEMAC-3D subroutine used to produce the results reported here are available from the corresponding author on request. The current implementation will be deposited on a public repository at the appropriate development milestone of a further framework extension.

Acknowledgments: The authors acknowledge funding from the EPSRC Impact Acceleration Account (EP/X525698/1) at the University of Edinburgh (PV097) through the CES:UPSTREAM Strategic Partnership project with Crown Estate Scotland. The second author acknowledges EPSRC CASE Studentship (C-00012428) sponsored by Sonardyne International Ltd. Access to the ARCHER2 UK National Supercomputing Service (https://www.archer2.ac.uk, accessed on 1 December 2025) is also gratefully acknowledged. During the preparation of this study, the authors used generative AI tools to assist in refining written expression for clarity, and improving the efficiency of data processing and implementation code. After using these tools, the authors critically reviewed, revised, and validated all content to ensure its accuracy, integrity, and originality. The authors take full responsibility for the content of the published article.

Conflicts of Interest: The authors declare no conflicts of interest. The funders had no role in the design of the study; in the collection, analyses, or interpretation of data; in the writing of the manuscript; or in the decision to publish the results.

Appendix A

A sensitivity analysis was conducted to bound the response of the wake-extension finding to uncertainty in the support structure drag coefficients (Table A1). Seven simulations were performed in an idealised rectangular channel ($50D \times 12D$ with a uniform 44.6 m depth), using the same turbulence closure, Nikuradse roughness, and source term implementation as the regional model. Horizontal fixed layers are used in the vertical discretisation (Figure 4) rather than sigma layers. A horizontal turbulence intensity of 8% was prescribed at the inlet, with a steady inflow velocity of 2.5 m/s. The drag coefficient of each component (tripod, tower, nacelle) was perturbed by $\pm 20\%$ in turn, holding the other two at their baseline values. The hub-height centreline velocity deficit was computed relative to a no-turbine ambient simulation in the same channel. The 5% deficit recovery distance $D_{5\%}$ was extracted for each case, and the resulting percentage change relative to the regional model baseline $\Delta D_{5\%}$ is reported.

Table A1. Sensitivity of the hub-height 5% velocity deficit recovery distance ($D_{5\%}$) to $\pm 20\%$ perturbations of the support structure drag coefficients, simulated in the idealised rectangular channel at an inflow velocity of 2.5 m/s. Values are reported as percentage changes relative to the baseline case as used in the regional model.

Case	$C_{d,\text{tripod}}$	$C_{d,\text{tower}}$	$C_{d,\text{nacelle}}$	$\Delta D_{5\%}$ (%)
Regional model baseline	0.75	1.05	0.90	—
Tripod-low	0.60	1.05	0.90	−1.4
Tripod-high	0.90	1.05	0.90	+1.4
Tower-low	0.75	0.84	0.90	−1.6

Table A1. *Cont.*

Case	$C_{d,\text{tripod}}$	$C_{d,\text{tower}}$	$C_{d,\text{nacelle}}$	$\Delta D_{5\%}$ (%)
Tower-high	0.75	1.26	0.90	+1.6
Nacelle-low	0.75	1.05	0.72	−1.8
Nacelle-high	0.75	1.05	1.08	+1.9

References

1. Sellar, B.G.; Wakelam, G.; Sutherland, D.R.; Ingram, D.M.; Venugopal, V. Characterisation of Tidal Flows at the European Marine Energy Centre in the Absence of Ocean Waves. *Energies* **2018**, *11*, 176. [CrossRef]
2. Black & Veatch. Lessons Learnt from MeyGen Phase 1A Final Summary Report. Technical Report. 2020. Available online: https://tethys-engineering.pnnl.gov/sites/default/files/publications/MeyGen-Lessons-Learnt-Full-Report.pdf (accessed on 30 April 2026).
3. Adcock, T.A.; Draper, S.; Willden, R.H.; Vogel, C.R. The Fluid Mechanics of Tidal Stream Energy Conversion. *Annu. Rev. Fluid Mech.* **2021**, *53*, 287–310. [CrossRef]
4. Orbital Marine Power. World's Most Powerful Tidal Turbine, the O2, Starts Exporting Clean Power. 2021. Available online: https://www.orbitalmarine.com/o2-power-generation/ (accessed on 30 April 2026).
5. Zhang, X.; Ji, R.; Sun, K.; Zhang, J.; Zhang, X.; Yin, M.; Kong, M.; Reabroy, R. A review of ocean tidal current energy technology: Advances, trends, and challenges. *Phys. Fluids* **2025**, *37*, 071308. [CrossRef]
6. Yin, M.; Ji, R.; Zhu, R.; Sun, K.; Zhang, J.; Cheng, Y.; Zhang, Y.; Reabroy, R. High-fidelity IDDES simulations of unsteady hydrodynamics and wake evolution characteristics of a tidal current turbine under focused wave-current interaction. *Renew. Energy* **2026**, *266*, 125647. [CrossRef]
7. Nishino, T.; Willden, R.H. The efficiency of an array of tidal turbines partially blocking a wide channel. *J. Fluid Mech.* **2012**, *708*, 596–606. [CrossRef]
8. Li, X.; Li, M.; Wolf, J.; Williams, A.J.; Badoe, C.; Masters, I. Local and regional interactions between tidal stream turbines and coastal environment. *Renew. Energy* **2024**, *229*, 120665. [CrossRef]
9. Stallard, T.; Collings, R.; Feng, T.; Whelan, J. Interactions between tidal turbine wakes: Experimental study of a group of three-bladed rotors. *Philos. Trans. R. Soc. A Math. Phys. Eng. Sci.* **2013**, *371*, 20120159. [CrossRef]
10. Gaurier, B.; Carlier, C.; Germain, G.; Pinon, G.; Rivoalen, E. Three tidal turbines in interaction: An experimental study of turbulence intensity effects on wakes and turbine performance. *Renew. Energy* **2020**, *148*, 1150–1164. [CrossRef]
11. Mycek, P.; Gaurier, B.; Germain, G.; Pinon, G.; Rivoalen, E. Experimental study of the turbulence intensity effects on marine current turbines behaviour. Part I: One single turbine. *Renew. Energy* **2014**, *66*, 729–746. [CrossRef]
12. Guerra, M.; Hay, A.E. Field observations of the wake from a full-scale tidal turbine array. *Renew. Energy* **2024**, *226*, 120315. [CrossRef]
13. Roc, T.; Conley, D.C.; Greaves, D. Methodology for tidal turbine representation in ocean circulation model. *Renew. Energy* **2013**, *51*, 448–464. [CrossRef]
14. Ramos, V.; Carballo, R.; Ringwood, J.V. Application of the actuator disc theory of Delft3D-FLOW to model far-field hydrodynamic impacts of tidal turbines. *Renew. Energy* **2019**, *139*, 1320–1335. [CrossRef]
15. Li, X.; Li, M.; McLelland, S.J.; Jordan, L.B.; Simmons, S.M.; Amoudry, L.O.; Ramirez-Mendoza, R.; Thorne, P.D. Modelling tidal stream turbines in a three-dimensional wave-current fully coupled oceanographic model. *Renew. Energy* **2017**, *114*, 297–307. [CrossRef]
16. Muchala, S.; Willden, R.H. Impact of tidal turbine support structures on realizable turbine farm power. *Renew. Energy* **2017**, *114*, 588–599. [CrossRef]
17. Rehman, Z.U.; Badshah, S.; Rafique, A.F.; Badshah, M.; Jan, S.; Amjad, M.; Rehman, Z.U.; Badshah, S.; Rafique, A.F.; Badshah, M.; et al. Effect of a Support Tower on the Performance and Wake of a Tidal Current Turbine. *Energies* **2021**, *14*, 1059. [CrossRef]
18. Zhou, J.; Guo, H.; Zheng, Y.; Zhang, Z.; Yuan, C.; Liu, B. Research on Wake Field Characteristics and Support Structure Interference of Horizontal Axis Tidal Stream Turbine. *Energies* **2023**, *16*, 3891. [CrossRef]
19. Zhang, Y.; Zhang, J.; Lin, X.; Wang, R.; Zhang, C.; Zhao, J. Experimental investigation into downstream field of a horizontal axis tidal stream turbine supported by a mono pile. *Appl. Ocean Res.* **2020**, *101*, 102257. [CrossRef]
20. Wei, M.; Liang, Z.; Chiew, Y.M. Vortex interactions in the near wake of a pile-supported horizontal axis tidal stream turbine. *Appl. Ocean Res.* **2025**, *165*, 104841. [CrossRef]
21. Afgan, I.; McNaughton, J.; Rolfo, S.; Apsley, D.D.; Stallard, T.; Stansby, P. Turbulent flow and loading on a tidal stream turbine by LES and RANS. *Int. J. Heat Fluid Flow* **2013**, *43*, 96–108. [CrossRef]

22. Faizan, M.; Badshah, S.; Badshah, M.; Haider, B.A. Performance and wake analysis of horizontal axis tidal current turbine using Improved Delayed Detached Eddy Simulation. *Renew. Energy* **2022**, *184*, 740–752. [CrossRef]
23. TELEMAC -3D Theory Manual V8P5. Technical Report. 2025. Available online: https://www.opentelemac.org/ (accessed on 30 April 2026).
24. Moulinec, C.; Denis, C.; Pham, C.T.; Rougé, D.; Hervouet, J.M.; Razafindrakoto, E.; Barber, R.W.; Emerson, D.R.; Gu, X.J. TELEMAC: An efficient hydrodynamics suite for massively parallel architectures. *Comput. Fluids* **2011**, *51*, 30–34. [CrossRef]
25. Hervouet, J.M. *Hydrodynamics of Free Surface Flows: Modelling with the Finite Element Method*; John Wiley and Sons: Hoboken, NJ, USA, 2007; pp. 1–341. [CrossRef]
26. Afgan, I.; Ahmed, U.; Apsley, D.; Stallard, T.; Stansby, P. ReDAPT-MD1.4 CFD Simulations of a Full-Scale Tidal Stream Turbine: Comparison Between Large-Eddy Simulations and Field Measurements. Technical Report. 2014. Available online: https://tidalenergydata.org/media/documents/MD1.4_CFD_Modelling_Part_4_-_Low_Flow_v1.3.pdf (accessed on 30 April 2026).
27. Lewis, M.; O'Hara Murray, R.; Fredriksson, S.; Maskell, J.; de Fockert, A.; Neill, S.P.; Robins, P.E. A standardised tidal-stream power curve, optimised for the global resource. *Renew. Energy* **2021**, *170*, 1308–1323. [CrossRef]
28. McNaughton, J. ReDAPT MC7.1–Initial Power Curve. Technical Report. 2014. Available online: https://tidalenergydata.org/media/documents/MC7.1_Initial_Power_Curve_A.pdf (accessed on 30 April 2026).
29. Mai, T. Estimation of Drag and Inertia Coefficients for a Tripod Support Structure of Offshore Wind Turbine. In *APAC 2019-Proceedings of the 10th International Conference on Asian and Pacific Coasts*; Springer Nature: London, UK, 2020; pp. 1091–1097. [CrossRef]
30. Arcigni, F.; Abhinav, K.A.; Collu, M.; Venturini, M. Analysis of tripod supported offshore wind turbines under conditions of marine growth. *Ocean Eng.* **2021**, *220*, 108441. [CrossRef]
31. DNV. DNV-RP-C205 Environmental Conditions and Environmental Loads. 2026. Available online: https://www.dnv.com/energy/standards-guidelines/dnv-rp-c205-environmental-conditions-and-environmental-loads/ (accessed on 30 April 2026).
32. Iiyama, T.; Furuya, M.; Arai, T.; Ui, A.; Okawa, R.; Shirakawa, K.; Shimada, T. Drag coefficient of circular cylinder in axial flow of water for a wide range of length to diameter ratios. *J. Nucl. Sci. Technol.* **2022**, *59*, 1478–1486. . . [CrossRef]
33. Almoghayer, M.A.; Lam, R.; Sellar, B.; Old, C.; Woolf, D.K. Validation of tidal turbine wake simulations using an open regional-scale 3D model against 1MW machine and site measurements. *Ocean Eng.* **2024**, *299*, 117402. [CrossRef]
34. UK Hydrographic Office. Seabed Mapping Service. 2020. Available online: https://www.admiralty.co.uk/access-data/seabed-mapping (accessed on 30 April 2026).
35. European Marine Observation and Data Network (EMODnet). Bathymetry. 2011. Available online: https://emodnet.ec.europa.eu/en/bathymetry (accessed on 19 September 2023).
36. Evans, L.; Ashton, I.; Sellar, B. Tidal turbine power performance assessments following IEC TS 62600-200 using measured and modelled power outputs. *Renew. Energy* **2023**, *212*, 138–150. [CrossRef]
37. Evans, L.; Ashton, I.; Sellar, B.G. Impact on Energy Yield of Varying Turbine Designs under Conditions of Misalignment to the Current Flow. *Energies* **2023**, *16*, 3923. [CrossRef]
38. OSU TPXO Tide Models. TPXO9-Atlas. 2026. Available online: https://www.tpxo.net/home (accessed on 19 September 2023).
39. Vennell, R.; Funke, S.W.; Draper, S.; Stevens, C.; Divett, T. Designing large arrays of tidal turbines: A synthesis and review. *Renew. Sustain. Energy Rev.* **2015**, *41*, 454–472. [CrossRef]
40. Robins, P.E.; Neill, S.P.; Lewis, M.J. Impact of tidal-stream arrays in relation to the natural variability of sedimentary processes. *Renew. Energy* **2014**, *72*, 311–321. [CrossRef]
41. Neill, S.P.; Litt, E.J.; Couch, S.J.; Davies, A.G. The impact of tidal stream turbines on large-scale sediment dynamics. *Renew. Energy* **2009**, *34*, 2803–2812. [CrossRef]